Discovery and recovery of crystalline materials with property-conditioned transformers

Cyprien Bone,* Matthew Walker, and Keith T. Butler[†]
Department of Chemistry, University College London,
20 Gordon Street, London WC1H 0AJ, United Kingdom

Kuangdai Leng

Earth Rover Program, 71-75 Shelton Street, Covent Garden, London, United Kingdom, WC2H 9JQ, United Kingdom

Luis M. Antunes
Independent Researcher, Canada

Ricardo Grau-Crespo

School of Engineering and Materials Science, Queen Mary University of London, London E1 4NS, United Kingdom

Amil Aligayev and Javier Dominguez

NOMATEN Centre of Excellence, National Centre for Nuclear Research, ul. A. So Itana 7, Otwock, 05-400, Poland

(Dated: November 27, 2025)

Generative models have recently shown great promise for accelerating the design and discovery of new functional materials. Conditional generation enhances this capacity by allowing inverse design, where specific desired properties can be requested during the generation process. However conditioning of transformer-based approaches, in particular, is constrained by discrete tokenisation schemes and the risk of catastrophic forgetting during fine-tuning. This work introduces CrystaLLM- π (property injection), a conditional autoregressive framework that integrates continuous property representations directly into the transformer's attention mechanism. Two architectures, Property-Key-Value (PKV) Prefix attention and PKV Residual attention, are presented. These methods bypass inefficient sequence-level tokenisation and preserve foundational knowledge from unsupervised pre-training on Crystallographic Information Files (CIFs) as textual input. We establish the efficacy of these mechanisms through systematic robustness studies and evaluate the framework's versatility across two distinct tasks. First, for structure recovery, the model processes high-dimensional, heterogeneous X-ray diffraction patterns, achieving structural accuracy competitive with specialised models and applications to experimental structure recovery and polymorph differentiation. Second, for materials discovery, the model is fine-tuned on a specialised photovoltaic dataset to generate novel, stable candidates validated by Density Functional Theory (DFT). It implicitly learns to target optimal band gap regions for high photovoltaic efficiency, demonstrating a capability to map complex structure-property relationships. CrystaLLM- π provides a unified, flexible, and computationally efficient framework for inverse materials design.

I. INTRODUCTION

Developing new functional materials has historically been a time-consuming process, with new materials applications often discovered serendipitously or promising candidates taking many decades of careful synthesis and characterisation before having tangible impacts[1]. There are many barriers that make discovery of new materials challenging, including navigating the vast compositional space of inorganic materials and effectively characterising newly synthesised candidates[2–5]. The combinatorial complexity of materials space, which scales exponentially with the number of elements, coupled with polymorphism and structural complexity, requires intelligent approaches to accelerating discovery[6–8]. Computational chemistry has helped ameliorate some of these problems by offering accurate predictions of the properties of new materials and complementing modern characterisation

techniques[9, 10]. However, accurate physics-based computations are generally too computationally expensive to allow for wide and fast explorations of materials space.

Generative artificial intelligence has emerged as a powerful tool for materials design [11–13]. In recent years, two main paradigms for generative materials modelling have emerged; diffusion/flow-based models, and transformer-based models[13-17]. Diffusion/flow approaches have achieved state-of-the-art performance in generating materials unconditionally (i.e. with no requirements other than to generate a plausible new material), and conditioned with compositional, or symmetry-based requirements[17-25]. They have also demonstrated conditioning on specific functional properties (e.g. magnetism)[26–29]. However, adapting these models to target physical properties beyond a narrow, predefined set remains difficult, often requiring substantial architectural changes and complete retraining[30]. Additionally, many diffusion and flow models rely on graph-based representations, where the computational cost of modeling inter-atomic relationships scales poorly with system size, limiting their applicability to large and complex chemistries[29].

^{*} cyprien.bone.24@ucl.ac.uk

[†] k.t.butler@ucl.ac.uk

Transformer-based generative models present an alternative framework for materials design, offering inherent architectural flexibility and favorable scalability of text-based representations for structure generation[31–36]. The self-attention mechanism at the heart of transformers[37] can contextualise varying levels of inputs, including compositional, structural, and functional property information. Functional property conditioning has been achieved with transformer-based large language models (LLMs) such as NatureLM and AtomGPT, which fine-tune general-use models, to guide crystal generation based on specified numerical properties like bulk modulus or X-ray diffraction patterns, using token-based guidance[38– 41]. Transformers face challenges conditioning on physical properties, as their discrete, digit-level tokenisation is fundamentally mismatched with continuous quantities[42, 43]. Standard tokenisation treats digits as independent categorical variables rather than continuous magnitudes, breaking the ordinal relationships in continuous data. As a result, the model struggles to interpolate values or grasp proximity in property space, a problem often compensated for with large amounts of data. While unlabeled structure datasets are constantly expanding (which lessens the problem for structure generation)[44–46], property-labeled datasets remain comparatively scarce. Hybrid architectures have also emerged, using flow matching to refine the discrete samples produced by large language models [47].

This work presents CrystaLLM- π (Property Injection), a transformer-based framework that aims to resolve these limitations. The main hypothesis is that we can introduce continuous representations of conditioning properties directly at the level of the attention mechanism, encouraging the model to attend to these requirements during inference and consequently generating desired materials more effectively. We introduce two mechanisms, Property-Key-Value (PKV) Prefix attention and the PKV Residual attention, which are referred to as Prefix and Residual methods from here. Both methods integrate continuous property information directly into the attention layers, bypassing sequence embedding layers. The mechanisms are designed to preserve the rich structural knowledge from the pre-trained base model, which mirrors CrystaLLM[48], while efficiently enabling structure generation controlled by functional property targets.

We begin by detailing the conditioning mechanisms, demonstrating that they effectively maintain the information learned from unsupervised pre-training on a large corpus of data without property labels, while effectively learning to condition from labeled datasets ranging from 1K to 600K materials. To isolate the impact of these architectural modifications, their generative performance is systematically evaluated against standard sequence-based conditioning baselines. We then demonstrate the generality of the methods, applying them to two important but vastly different materials design tasks. First, the recovery of known experimental structures from XRD data, where the Residual mechanism effectively processes variable-sized heterogeneous diffraction inputs. Then, generation of novel photovoltaic candidates, fine-tuned on a specialised dataset of around 5.3K materials with their asso-

ciated efficiencies. The physical viability of these generated candidates are confirmed through high-fidelity Density Functional Theory (DFT) calculations.

The results establish inverse design capabilities of conditional autoregressive crystal structure generation. CrystaLLM- π provides an accessible, lightweight and flexible framework for both the recovery and discovery of crystalline materials with a range of targeted functional properties and structural prompts, which can be adapted to a wide range of scenarios in materials design without the need for complex architectural re-design or extensive re-training. The results lay the foundation for further application of transformer-based models to important tasks throughout the materials design pipeline.

II. RESULTS

A. CrystaLLM- π Framework

CrystaLLM- π is a generative framework for material discovery, designed to sequentially produce Crystallographic Information Files (CIFs). The framework's backbone employs a GPT-2 transformer architecture, similar to the original CrystaLLM paper[48, 49]. The model is trained to autoregressively generate chemically plausible crystal structures by learning the syntax and physical constraints present in crystallographic data, the mechanisms of which are extensively discussed in the original paper[48].

CrystaLLM- π is an adaptation of the original framework to condition the generation of crystal structures on target functional properties. It incorporates several modifications: the model was implemented on the Hugging Face platform, the unlabeled CIF dataset was expanded, a new batching mechanism was engineered to allow for conditioning, and boundary tokens and a CIF format-aware loss function were implemented (see Methods IV B). To isolate the cumulative effect of modifications, CrystaLLM- π was benchmarked without functional property conditioning to validate core crystal structure prediction (CSP) capabilities of the updated framework. The results on the original paper's challenge set task (Appendix Table V D) which evaluate CSP performance on complex, experimentally validated structures, confirm that the adapted backbone performs comparably to its predecessor, with performance metrics within $\pm 4.1\%$ points.

To overcome the limitations of current conditional generation models, as well as transformer-specific challenges detailed in the introduction, CrystaLLM- π incorporates a conditioning framework, shown in Figure 1. The objective is to address the inefficient discrete representation of continuously valued functional properties and to attend to conditioning throughout the generation process. This is achieved by developing a conditioning encoder that bypasses discrete tokenisation, and property information that is injected directly into the modified attention mechanism[42, 43, 50].

The training objective, seen in Figure 1a, is to model the conditional probability distribution of a next token given the pre-

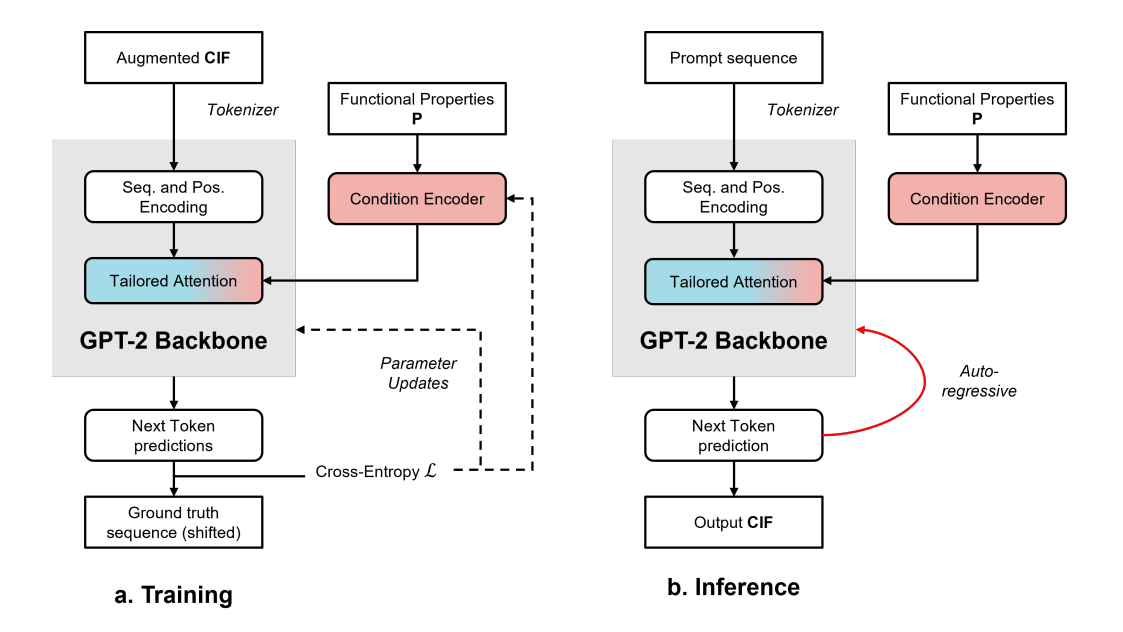


Figure 1. An overview of the property conditioned crystal structure generation framework. **a.** The training process involves optimising the model's parameters to predict the subsequent token in a given CIF sequence. This prediction is conditioned on previous tokens in the CIF sequence and a learned embedding from target functional properties *P*, which is injected into each multi-head attention layer. **b.** The inference process uses a prompt and a target property vector to autoregressively generate a complete CIF by iteratively sampling and appending the next predicted token.

ceding sequence and a set of target properties *P*. An input CIF is tokenised and converted into a sequence of embeddings with positional encodings. Simultaneously, the Condition Encoder projects the numerical properties into a continuous conditioning embedding. This embedding is injected into each multihead attention (MHA) layer of the GPT-2 backbone, biasing the generation process. For each token, the model outputs a probability distribution over the vocabulary. A Cross-Entropy loss (See Methods IV B) is then computed between this distribution and the ground-truth sequence, which is shifted by one position to serve as the prediction target. The loss is backpropagated to optimise both the parameters of the backbone and the encoder.

During inference (Figure 1b), a target property vector and an initial prompt sequence are provided. Prompting flexibility allows generation of materials given as much structural information as desired, including ab-initio (no compositional information provided), cell composition only or cell composition and space-group. Subsequent tokens are autoregressively generated by sampling from the models output probability distribution which considers both sequence and property-level representations. The sampled token is fed back into the input for the next step iteratively, until a complete CIF is produced.

B. Architectures for Property-Conditioned Generation

To tackle the challenge of a flexible framework which conditions structure generation on functional properties, we implemented and benchmarked four distinct architectures. These methods were all designed to integrate a numerical condition

vector, $\mathbf{c} \in \mathbb{R}^P$ where P is the number of properties, to guide the generative process. They are grouped into two classes: sequence-level methods and tailored attention mechanisms developed for this work.

Preserving the extensive structural knowledge from unsupervised pre-training is critical in conditional fine-tuning to mitigate catastrophic forgetting[51]. For this goal, a dual optimisation strategy was developed and applied, detailed in Methods IV C. A conservative learning rate is applied to the pre-trained backbone parameters to favour retention of foundational knowledge, while a higher learning rate is used for the newly initialised conditioning layers to accelerate adaptation to the new task.

1. Sequence-Level Conditioning

We first implemented two methods that modify the model's input sequence, serving as comparative baselines to the tailored attention methods.

The **Raw Conditioning** method involves the direct, digitlevel tokenisation of the numerical values in the property vector $\mathbf{c} \in \mathbb{R}^P$. This resulting sequence of M tokens (where $M \geq P$, one token per digit for each condition) is prepended to the tokenised input sequence $\mathbf{x} = (x_1, \dots, x_L)$. Formally, if we denote the tokenised property string as $\mathbf{t}_{props} = (t_1, \dots, t_M)$, the new input sequence becomes $\mathbf{x}' = (<\mathsf{bos}>, t_1, \dots, t_M, \setminus n, x_1, \dots, x_L, <\mathsf{eos}>)$. As this approach only manipulates the input sequence, it requires no architectural modifications and handles the property values as discrete tokens.

From the hypothesis that a continuous embedding for the properties is more naturally suited to the task, the **Prepend Conditioning** method introduces a learned, continuous representation of **c**. A **Prepend Encoder**, implemented as a multi-layer perceptron (MLP) with ReLU activation, projects **c** into a sequence of P condition embeddings, $\mathbf{E}_c \in \mathbb{R}^{P \times d_{\text{emb}}}$, where d_{emb} is the model's embedding dimension. The input to the transformer is the concatenation of these condition embeddings with the standard token embeddings, $\mathbf{E}_x \in \mathbb{R}^{(L+P) \times d_{\text{emb}}}$. The regular attention mechanism (A_{out}) operates on this concatenated sequence:

$$A_{\text{out}}(Q_{\text{seq}}, K_{\text{seq}}, V_{\text{seq}}) = \operatorname{softmax}\left(\frac{Q_{\text{seq}}K_{\text{seq}}^{\mathsf{T}}}{\sqrt{d_k}}\right)V_{\text{seq}}$$
 (1)

where $Q_{\rm seq}$, $K_{\rm seq}$, and $V_{\rm seq}$ are the Query, Key, and Value matrices, respectively, generated from the transformer's representation of the concatenated sequence containing both token and condition embeddings. The full architecture diagram can be found in Appendix V F.

2. Tailored Attention Conditioning

To address the hypothesis that direct manipulation of the attention mechanism by continuous property representations would be more effective to strengthen targeted generation than sequence-level conditioning[50], we developed two architectures, Prefix and Residual, which incorporate property information directly into the transformer's decoder blocks. Intuitively, the Prefix architecture extends the effective context window by concatenating learned property keys and values to the sequence, imposing a 'hard' structural bias. On the other hand, the Residual architecture operates as an additive modification to the base self-attention, injecting a parallel property-based score dynamically. This is effectively a weighted residual term that 'softly' steers the generation without disrupting the intrinsic sequence attention operations.

Prefix attention conditioning (Figure 2) directly injects property information into the self-attention mechanism of each transformer layer, bypassing the sequence encoding. This is achieved by generating a set of 'ghost' Key-Value (KV) pairs from the condition vector, which are then concatenated with the KV pairs derived from the input sequence. This method is an adaptation of Li and Liang's Prefix Tuning method[50].

The **Prefix Encoder** (See Appendix V E) transforms the input condition vector $\mathbf{c} \in \mathbb{R}^P$ into a tensor compatible with the attention mechanism. The vector \mathbf{c} is first projected to a higher dimensional latent space via a linear layer, followed by Layer Normalisation and ReLU. This hidden representation is projected to the KV tensor dimension for all attention heads and layers, $\mathbf{h}_{\mathrm{KV}} \in \mathbb{R}^{P \times N \times h \times 2 \times d_k}$, where P is the number of conditions, N being the number of decoder blocks, h the number of attention heads, and $2 \times d_k$ the dimension of the KV pair matrix. The resulting tensor is split into Key (K_{Prefix}) and Value (V_{Prefix}) tensors.

For each layer, the attention mechanism is modified. Given Q_{seq} from the input sequence, the attention output is computed as:

$$A_{\text{out}}(Q_{\text{seq}}, K, V) = \operatorname{softmax}\left(\frac{Q_{\text{seq}}(K^{\top})}{\sqrt{d_k}}\right)V$$
 (2)

where $K = [K_{\text{Prefix}}; K_{\text{seq}}]$ and $V = [V_{\text{Prefix}}; V_{\text{seq}}]$ are the concatenations of the conditioning and sequence derived Key and Value matrices, respectively.

Residual attention conditioning (Figure 2) introduces a more nuanced, 'soft' conditioning mechanism that dynamically weights the influence of the property conditions. The Residual Encoder (See Appendix V E) is architecturally similar to the Prefix Encoder but employs tanh activations and utilises reshaping and einsum operations for more structured transformations. These are engineered so each of the P conditions initially influence a dedicated portion of the latent space before being combined. The output of the encoder is a set of KV pairs, K_{Residual} and V_{Residual} , where each pair can be attributed to an input condition. This structured encoding preserves the associativity between each of the P conditions and its resulting KV pair, distinct from the Prefix approach where property representations are collectively projected.

The core of this method is the **Residual Attention** module. For each attention head, two separate attention scores are computed in parallel: a standard self-attention score over the input sequence ($A_{\rm base}$) and a 'Residual' attention score ($A_{\rm Residual}$) between the input sequence's Queries ($Q_{\rm seq}$) and the Residual Keys ($K_{\rm Residual}$) and Values ($V_{\rm Residual}$). These are then combined via a learned, per-layer weighting parameter, α . The modified attention output, $A_{\rm out}$, is computed as:

$$A_{base} = \operatorname{softmax} \left(\frac{Q_{\text{seq}} K_{\text{seq}}^{\mathsf{T}}}{\sqrt{d_k}} \right) V_{\text{seq}}$$

$$A_{\text{Residual}} = \operatorname{softmax} \left(\frac{Q_{\text{seq}} K_{\text{Residual}}^{\mathsf{T}}}{\sqrt{d_k}} \right) V_{\text{Residual}}$$

$$A_{\text{out}} = A_{\text{base}} + \alpha \cdot A_{\text{Residual}}$$
(3)

The scalar weight, α , is initialised at zero, similar to the 'zero-initialisation' technique used in Low-Rank Adaptation (LoRA) fine-tuning[52]. This ensures that the model initially relies only on the pre-trained self-attention mechanism, preserving its generative capabilities and mitigating catastrophic forgetting. Optimisation of α during training dynamically calibrates the degree of conditioning.

This architecture handles missing or unspecified conditions, a capability enabled by the Residual Encoder's associativity and the parallel, additive structure of the attention layer. When a value of -100 is used in the condition vector \mathbf{c} , the attention scores (computed as $Q\cdot K_{\mathrm{Residual}}^{\mathsf{T}}$) for queries attending to that specific condition variable are set to $-\infty$, effectively nullifying its contribution after softmax in A_{Residual} , similarly to regular attention masking. The additive design bypasses an important limitation of Prefix conditioning for masking 'missing' conditions. By concatenating keys, Prefix effectively changes the se-

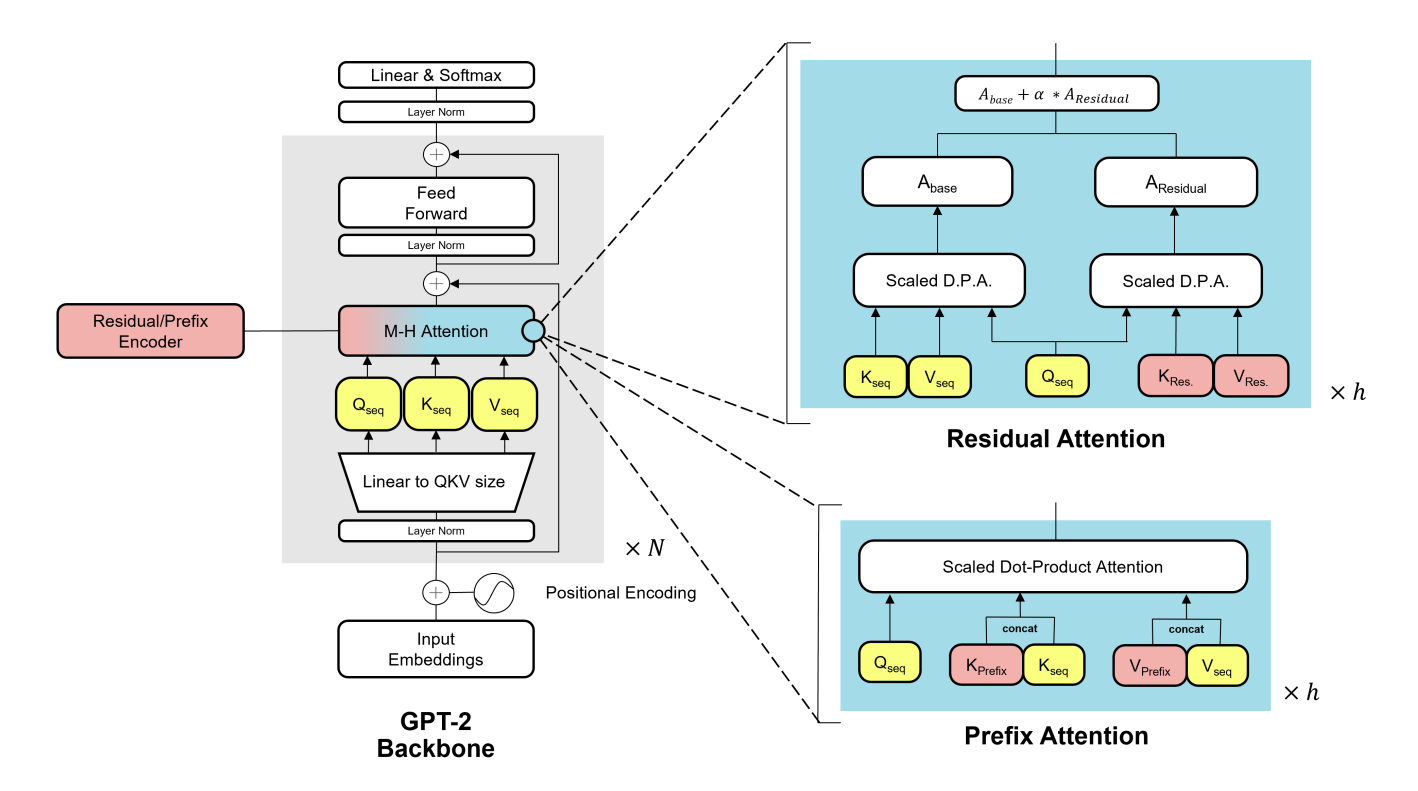


Figure 2. Prefix and Residual Conditioning method architectures. The Prefix and Residual Encoders (See Appendix VE for details) handle the transformation of the property condition vector into an embedding of the same size as the attention's Key-Value tensors. These are injected directly to the attention layers of the transformer, where the modified mechanism allows for attention to both conditions and sequence, for property aware generation of CIFs. N Represents the number of decoder blocks, and h is the number of attention heads. α is the learned Residual attention scaling parameter from Equation 3.

quence length, altering the softmax normalisation. The residual architecture avoids this perturbation, allowing 'missing' condition handling while maintaining the crystal sequence's intrinsic attention distribution.

C. Validation of the Conditioning Frameworks

Having established the four conditioning architectures in Section II B, their performance was quantitatively validated. Firstly, we assess the transferability of unsupervised learning on unconditional CIF generation to the conditional 'labeled' setting. Then, we quantify the performance gain from continuous encoder representations over discrete tokens and compare the efficacy of sequence-level versus attention-based conditioning. Finally, we evaluate how the most promising methods respond to different dataset sizes, representing realistic research settings.

1. Advantages of pre-training and condition encoding

Figure 3 shows the performance of the four conditioning architectures on the task of generating a crystal with a specified band gap. The property is varied systematically from 0 to $12 \, eV$ representing a range across the distribution of materials

in the training set, which has a high density at $0\,eV$ and effectively zero density beyond $8\,eV$; this distribution is shaded on the plots. We assess the fraction of generated materials with the desired gap (a), with chemically valid structures (b) and with high quality structures (c) across the conditioning range. Validity is assessed based on symmetry, bond length, and atom site multiplicity constraints (see Methods IV E 1). Quality is assessed by the VSUN metric which incorporates Validity, Uniqueness, Novelty and Stability of generated structures, similarly to the metric introduced by Zeni et al.[30] We compare pre-trained and from-scratch models for all four conditioning approaches, where the pre-training dataset is the LeMaterial dataset (4.35M structs) and the fine-tuning/scratch dataset is the MP Bandgap (53.3K) (See Methods IV A).

The utility of pre-training is clearly demonstrated, yielding an average increase of $20.4 \pm 2.1\%(SE)$ in Validity and $14.4 \pm 0.9\%(SE)$ in VSUN for the generated structures. The models are able to generate materials with properties beyond the dense regions of the training distribution (at $6.42\,eV$ for example), showcasing a capacity for extrapolation. While there are some improvements in Hit-Rate using pre-trained models, the main advantage of pre-training is clearly in the increased generation of valid, high-quality structures, as indicated in panels (**b**) and (**c**) of Figure 3.

This generative reach is, however, dependent on the distribu-

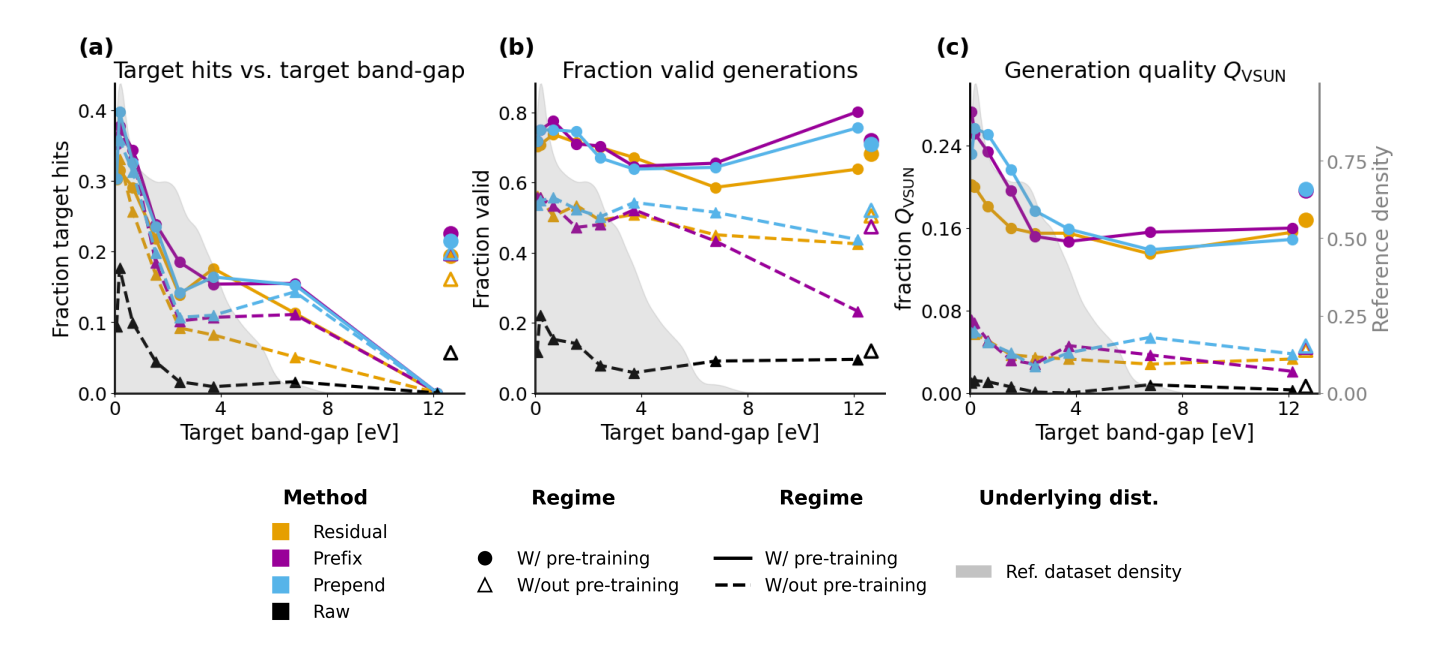


Figure 3. Study of how various conditioning methods are affected by starting with a pre-trained model or not with respect to the following metrics: Hit-Rate for a target compared to the desired band gap (a), evolution of valid structure amount (b) and quality (c). Metrics are compared for each method with 1K generation attempts at different conditioning targets (See Appendix V G for exact target values), labeled with markers. The generation quality (Q_{VSUN}) is a metric which groups the Validity, Stability, Uniqueness and Novelty (VSUN) metrics, which is true if all these are satisfied (Structural Novelty is measured here, Methods IV E for additional details). The icons to the right side of each plot represent the mean fraction of the conditioning methods over all targets, indicating overall performance. For each of the sub-panels, the frequency of band gaps seen during training is presented in grey.

tion of properties seen in training. The Hit-Rate for matching the target band gap in (a) is strongly correlated with the training data density (r=0.78), indicating that generation in extreme and sparsely populated regions remains a challenge. In contrast, Validity and Quality show weak correlation with the data distribution (r=0.173 and 0.216 respectively), which suggests the models prioritise structural soundness over meeting a property target that would result in a chemically implausible structure.

The Raw baseline conditioning method is excluded from further study due to its consistent underperformance. While the from-scratch version was already substantially inferior to other methods, highlighting inferior performance of tokenlevel conditioning, the pre-trained Raw model failed to generate any valid structures. This is likely because the direct insertion of conditioning tokens creates a disruptive input format change that the model cannot adapt to after pre-training, a hypothesis supported by the severe loss-landscape perturbation shown in Appendix VH. Increasing the size of the finetuning dataset or the learning rate may have resolved this issue, but the latter would come at the cost of substantially shifting pre-trained model weights, which would reduce the amount of pre-training information preserved. Therefore, given the demonstrated benefits of pre-training and the instability of the Raw approach, our subsequent analysis focuses on the three superior *pre-trained* models with continuous property encoding: Prepend, Prefix, and Residual.

2. Advantages of attention-level conditioning

This analysis conditions on the Mattergen Density fine-tuning dataset (653K labeled structures), a structural property available a priori for all materials, with results presented in Figure 4. The findings demonstrate that the Prefix architecture is the most effective conditioner across the different dataset sizes. The MAE for the density of generated structures over all targets using Prefix was $5.26 \pm 1.51 \,\mathrm{g/cm^3}(SE)$ compared to $6.19\pm1.68 \text{ g/cm}^3(SE)$ and $6.35\pm1.66 \text{ g/cm}^3(SE)$ for Prepend and Residual respectively. Given the overlapping standard errors, paired t-tests were also calculated which show that the enhanced performance of Prefix is statistically significant, with p-values of 0.005 and 0.002 for improvement with respect to Prepend and Residual models. This is further supported by the lower average standard deviation in its generated distributions $(1.79 \text{ g/cm}^3 \text{ for Prefix vs } 1.99 \text{ g/cm}^3 \text{ and } 1.96 \text{ g/cm}^3)$ for Prepend and Residual), indicating higher generation confidence.

Interestingly, a different trend is observed when fine-tuning data is scarce. In the 1K structure training data case, the Residual model outperforms Prefix and Prepend for Valid structure generation (y-coordinate of the icons), generating on average $880.7 \pm 15.6(SE)$ valid structures followed by Prefix with $818.0 \pm 13.1(SE)$ and finally Prepend with $729.7 \pm 12.1(SE)$. The Residual method's training loss evolves continuously from the pre-training phase, indicating a smooth integration of con-

ditioning information. In contrast, Prefix and Prepend exhibit a distinct initial jump in loss, signifying a more disruptive shift. This smoother transition for Residual likely mitigates catastrophic forgetting, preserving pre-trained knowledge and leading to higher validity rates. This conjecture is supported by the fine-tuning dynamics shown in Figure V H.

Through these two validation studies, the attention-modified methods show distinct advantages over sequence-based conditioning. The Prefix model stands out as a 'harder' conditioning method, able to generate structures steered the most strongly towards designed conditions, and maintained validity rates higher than Prepend conditioning in scarce dataset regimes. Then, Residual is a 'softer' alternative which is the best at maximising information retention compared to the other two methods when less fine-tuning data is available. The benefit of this 'softness' is further extended by the fact this method handles missing condition values in the training dataset, meaning it can train and generate on heterogeneous property data labels when the other methods cannot.

D. Recovery of materials using X-Ray Diffraction information conditioning

Beyond generating structures from scalar functional properties, the flexibility of the CrystaLLM- π conditioning framework is validated on the more complex task of structure recovery from high-dimensional conditioning vectors. Here, the Residual model interprets a condition vector of heterogeneous numerical data, which is made up of the 20 most intense X-ray diffraction (XRD) peak positions and their associated 20 intensities. Vectors with fewer than 20 diffraction peaks have the remaining values padded with a 'missing' value (-100). XRD is a primary technique for characterising inorganic crystals, providing data on structure periodicity and atomic distribution. The determination of an exact crystal structure from diffraction data is a challenging problem because of intrinsic issues like peak overlap, phase impurities, and the difficulty of resolving low-scattering atoms[53]. Traditional algorithms for this task often require extensive prior information, such as space-group or known structural units[54], motivating the development of ML models for strong data-driven propertystructure mappings.

1. Benchmarking against other ML models for XRD conditioned generation

To validate this capability, the framework is first benchmarked against concurrently developed generative models for structure determination conditioned on XRD data. This includes DiffractGPT, a general-purpose LLM fine-tuned for XRD data using prompt engineering[40]; Uni3Dar, an autoregressive model using compressed spatial tokens with multi-modal conditioning tokens[55]; and PXRDGen, a diffusion pipeline leveraging contrastive learning to condition generation[56]. Model performance is evaluated on the MP-20[57] and Jarvis-DFT[58] benchmarks.

To ensure a rigorous and transparent comparison despite the heterogeneity of existing benchmarking protocols, specific methodological adjustments were necessary. For Jarvis-DFT, the original data splits were unavailable, requiring the generation of a reproducible random 90/10 split. Furthermore, we identified that standard validity screens in benchmarks like MP-20 filtered out 8.93% of the matching test structures (a problem also addressed in the PXRDGen paper [56]). To decouple the generative model's intrinsic performance from these external heuristic filters, we report metrics both with and without these screens for MP-20.

For the MP-20 benchmark, CrystaLLM- π was trained from scratch following the PXRDGen protocol. In the same manner as Uni3Dar, we employed a perplexity-based ranking to select the most confident prediction (see '1-perplexity' in Methods IV E). Performance is presented in Table I. CrystaLLM- π achieves a competitive conditional match rate of 62.73% and an RMS-d of 0.0444, representing a 37.2% improvement in structural quality over PXRDGen (0.0707) for matched structures.

However, direct comparison is complicated by the studied limitations of the benchmark's validation protocol[59]. By bypassing the validity screen for example (Table I, 'Skip Valid.'), the match rate increases to 69.01%, demonstrating that the model effectively recovers structures that are otherwise discarded by the benchmark's pre-filtering.

Model	Condit	ional	Unconditional		
1710401	Match %	RMS-d	Match %	RMS-d	
PXRDGen	68.68	0.0707	-	-	
Uni3Dar	75.08	0.0276	65.48	0.0317	
CrystaLLM- π	62.73	0.0444	55.85	0.0437	
CrystaLLM- π					
(Skip Valid.)	69.01	0.0465	-	-	

Table I. Performance on the MP-20 benchmark with PXRD guided crystal structure prediction. Best metric is reported in bold and second best in italics. All true structures are evaluated to 1 structure. PXRDGen uses a 1-shot generation approach, while Uni3Dar and CrystaLLM- π use '1-perplexity' ranking. For unconditional metrics, we use the reported metrics for the '1-shot' MP-20 benchmark from Antunes et al.[48]. The 'Skip Valid.' row reports results when the benchmark's structure validity screen is bypassed during matching, offering a view of performance unconstrained by heuristic filtering of ground truth data.

The framework was evaluated on the Jarvis-DFT benchmark following the DiffractGPT protocol[40]. To ensure reproducibility in the absence of public splits, we fine-tuned the pre-trained CrystaLLM- π model on a generated 90/10 split. Consistent with our MP-20 analysis and because no filter was mentioned in the original Jarvis-XRD benchmark, we bypassed pre-matching validity screens to avoid arbitrarily filtering potential matches.

Table II compares performance against Gradient Boosting (GBR), CNN, and DiffractGPT baselines. CrystaLLM- π generations demonstrate superior structural accuracy. The top

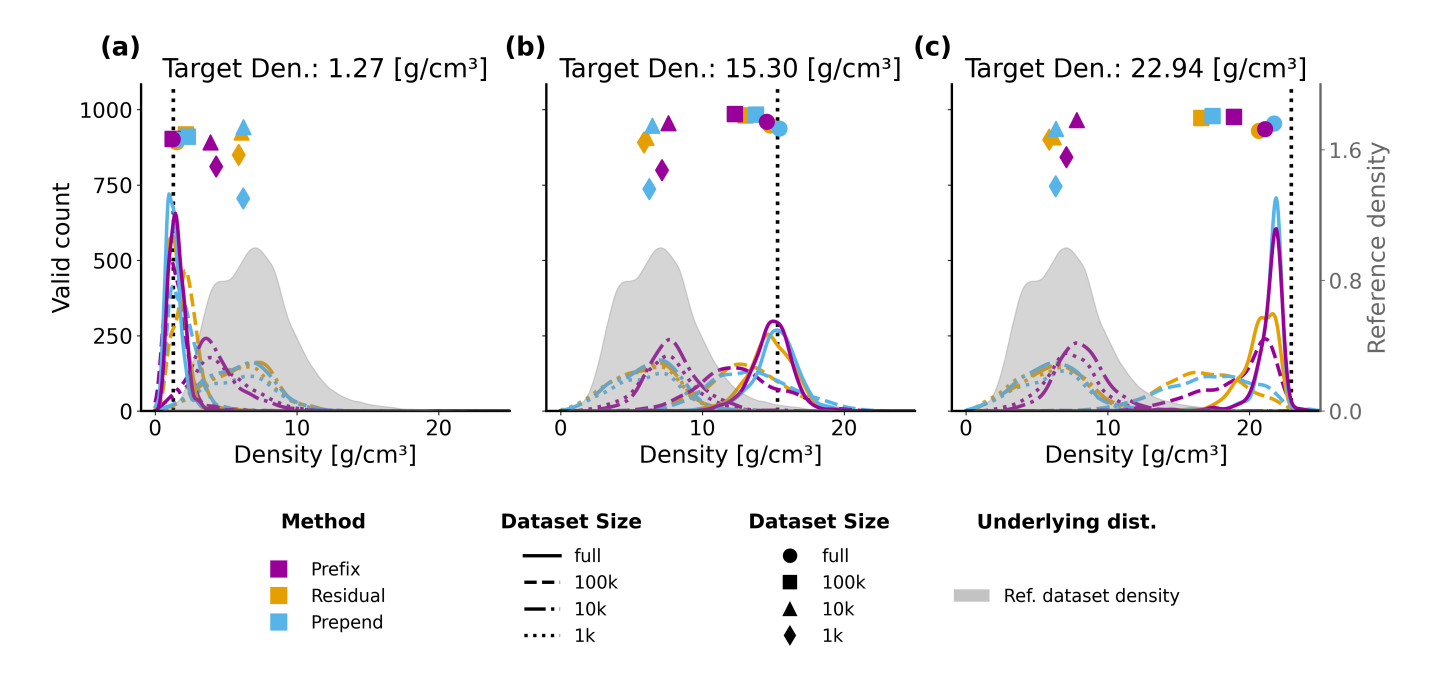


Figure 4. Effect of dataset size on density conditioned generation capabilities across three different methods and four different dataset sizes. Each sub-panel represents a different conditioning target (dotted line parallel to the y-axis), where each curved line informs on the distribution of structure density for the generated materials given a target, method and dataset size. Icons above the lines represent mean density (x-axis) and total valid count (y-axis) for each condition. For each of the sub-panels, the frequency of density values seen during training is presented in grey.

perplexity-ranked structure (see Section IV D for description of this ranking) achieves an RMS-d of 0.0347, a 50.4% reduction compared to DiffractGPT (0.07). This fidelity is confirmed by the lowest Mean Absolute Error (MAE) across all lattice parameters (0.096 $^{\circ}A$, 0.098 $^{\circ}A$ and 0.183 $^{\circ}A$ for a,b,c respectively). When allowing 20 consistent generation attempts per structure, the match rate reaches 85.47% while maintaining a low RMS-d of 0.0361.

Model	Match %	RMS-d	MAEa	MAE b	MAEc
- Iviouci	Witten 70	TENID U	WINID W	171111111111111111111111111111111111111	TVIII C
GBR	-	-	1.030	0.990	1.270
CNN	-	-	0.280	0.270	0.280
DiffractGPT					
(formula)	-	0.0700	0.170	0.180	0.270
CrystaLLM- π					
(20-consistent)	85.47	0.0361	0.142	0.135	0.216
CrystaLLM- π					
(1-perplexity)	66.22	0.0347	0.096	0.098	0.183

Table II. Performance on the Jarvis-DFT benchmark. Best metric is reported in bold and second best in italics. CrystaLLM- π results are shown for the highest ranked perplexity output per structure ('1-perplexity'), as well as results allowing matching for 20 consistent structures per true test set material ('20-consistent'). MAE values refer to the lattice parameters of the best matched structures.

While absolute metrics are sensitive to protocol choices, the aggregate performance confirms that CrystaLLM- π achieves structural fidelity competitive or superior to specialised ar-

chitectures. Having validated the model on ideal theoretical datasets, its practical utility is next evaluated on the more challenging task of recovering structures from the Crystallography Open Database (COD) using experimental XRD data.

2. Experimental Structure Recovery from COD Data

We evaluated the model on a challenging test set of 198 unseen experimental materials and XRD data from COD. This set aligns with realistic research, featuring broader and more complex prototypes as well as minor disorder or impurities not found in theoretical data. Because the model cannot generate disordered structures in its current form, we task the model with generating the ordered counterpart of structures with minor disorder (See Appendix V A). The XRD-conditioned model was compared against an unconditioned baseline, which is the same fine-tuned Residual model given 'missing' conditions during inference, showing the method's flexibility at inference. Metrics for non-matched structures were also included to evaluate model behaviour on the whole test set.

The results for 3 identical experiment runs, presented in Figure 5, demonstrate a clear capability for recovering experimental structures. When provided with XRD conditioning and allowed matches over '20-consistent' generations, the model achieved an average structure match rate of $44.78\pm0.73\%(SE)$. The unconditioned model also performed competently with a match rate of $42.26\pm0.61\%(SE)$, likely owing to XRD information seen during fine-tuning which bi-

ases the learned probability distribution. However, providing XRD data during inference offers advantages beyond the small increase in recovery rate.

A primary benefit of conditioning is the enhanced fidelity of the predicted lattice parameters. As shown in the scatter plots (a) and (b), conditioning leads to a tighter correlation between predicted and target values for all structures, including those not matched. Conditioning reduces the MAE across lattice parameters a, b, c by an average of $0.25 \pm 0.068\,^{\circ}A$ (SE). Additionally, the coefficient of determination (R^2) for these parameters improves by an average of 0.133 ± 0.042 (SE), confirming a more robust and physically realistic unit cell prediction.

Next, conditioning gives an advantage in computational efficiency. Generating '20-consistent' structures for the entire test set required on average 1 hour and 20 minutes for the unconditioned model, whereas the conditioned model completed the same task in just 28 minutes, a 2.9-fold reduction in computation time. This reduction in computing time indicates that the experimental XRD pattern acts as a powerful 'guiding' tool in the vast chemical space. Such guidance is particularly valuable for complex or novel materials where the model's unconditional prior may be weak, allowing it to converge on sensible structure candidates with greater speed and reliability.

The model's average perplexity shows the trade-off between chemical priors and external constraints. The unconditioned model exhibits a lower perplexity, suggesting high confidence based on its learned structural priors. In contrast, the conditioned model seems to balance its priors with the external constraints imposed by the XRD data. This would push the model to more 'uncertain' predictions at each generative step, resulting in higher perplexity.

3. Experimental Structure Recovery for TiO₂ polymorphs

To test the model's ability to resolve structurally similar polymorphs, an important challenge for XRD analysis, we evaluated its performance on three experimental TiO_2 polymorph XRD patterns. This test included varying levels of novelty: Rutile and Anatase were seen with theoretical XRDs during the first fine-tuning phase, while Brookite was absent from all training and fine-tuning.

As shown in Table III, CrystaLLM- π successfully recovers the desired polymorphs from input cell composition and XRD conditioning within '20-consistent' attempts. It is important to note that while all polymorphs share the same reduced formula (TiO₂), they differ in unit cell composition. In the training data, the specific stoichiometry of Rutile's unit cell (Ti₂O₄) is associated only with the rutile structure. However, the unit cell compositions for Anatase (Ti₄O₈) and Brookite (Ti₈O₁₆) are not unique, the training set contains other distinct polymorphs sharing these atom counts.

The number of matches (N Matches) and RMS-d follow expected trends. Accuracy is highest when the unit cell composition has only one structure (Rutile), decreases when the

unit cell composition is shared with other known polymorphs (Anatase), and decreases further when the specific polymorph structure is completely novel to the model (Brookite). Furthermore, predictive difficulty scales with system complexity where matches decrease as cell size and XRD pattern complexity increase. This is illustrated in Appendix V M, which overlays theoretical, experimental, and best-guess XRD patterns.

Notably, adding the space-group to the prompt, requiring no pipeline modification, increased average recovery to $96.67 \pm 2.89\%$ out of 20 attempts across all 3 polymorphs. This confirms a progression of predictive capability as more information is fed to the model. Limitations were observed when prompting with $2\times$ the base stoichiometry. The model does not generate the expected supercell, suggesting this concept was not learned, as the training data lacked supercell configurations.

TiO ₂ Polymorph Theor. XRD seen	Rutile Yes	Anatase Yes	Brookite No
Prompts	N Matches (RMS-d)	N Matches (RMS-d)	N Matches (RMS-d)
Comp.	$15 (5.17 \times 10^{-5})$	2 (0.0285)	1 (0.485)
Comp. + s.g	$20 (1.62 \times 10^{-4})$	$19 \ (4.33 \times 10^{-4})$	19 (0.344)
SC Comp.	0	0	0
SC Comp. + s.g	0	0	0

Table III. Comparison of matching metrics for TiO₂ polymorphs (Rutile, Anatase, and Brookite). No experimental TiO₂ structures or XRD data were ever seen during model training. For Anatase and Rutile, the theoretical XRD and structures were seen during the first fine-tuning step, while Brookite was never seen during training. The metrics reported are number of matches for '20-consistent' attempts and the RMS-d for the best matching structure in parentheses. The rows represent different prompts for various experimental scenarios, where we analyse the case of having a cell composition, a cell composition and space-group (s.g) and for both of these when the model is prompted with double stoichiometry (SC - Supercell Composition).

E. Exploration of photovoltaic efficiency chemical space

The Spectroscopic Limited Maximum Efficiency (SLME) serves as a theoretical measure of photovoltaic potential, integrating absorption profiles, band gap nature, and non-radiative recombination losses to estimate the upper limit of power conversion efficiency[60, 61]. Identifying materials with high SLME is a difficult task as it requires navigating a multi-objective optimisation landscape where optimal implicit electronic structure and optical properties need to be simultaneously considered. We investigate whether the CrystaLLM- π framework can leverage large-scale unsupervised pre-training to map complex structure-property relationships in a data-scarce regime. The model was fine-tuned on the MP-SLME dataset[62], with 5.35K inorganic structures labeled with SLME values. Generation was conditioned on the maximum observed SLME in the training set (33.2%) to

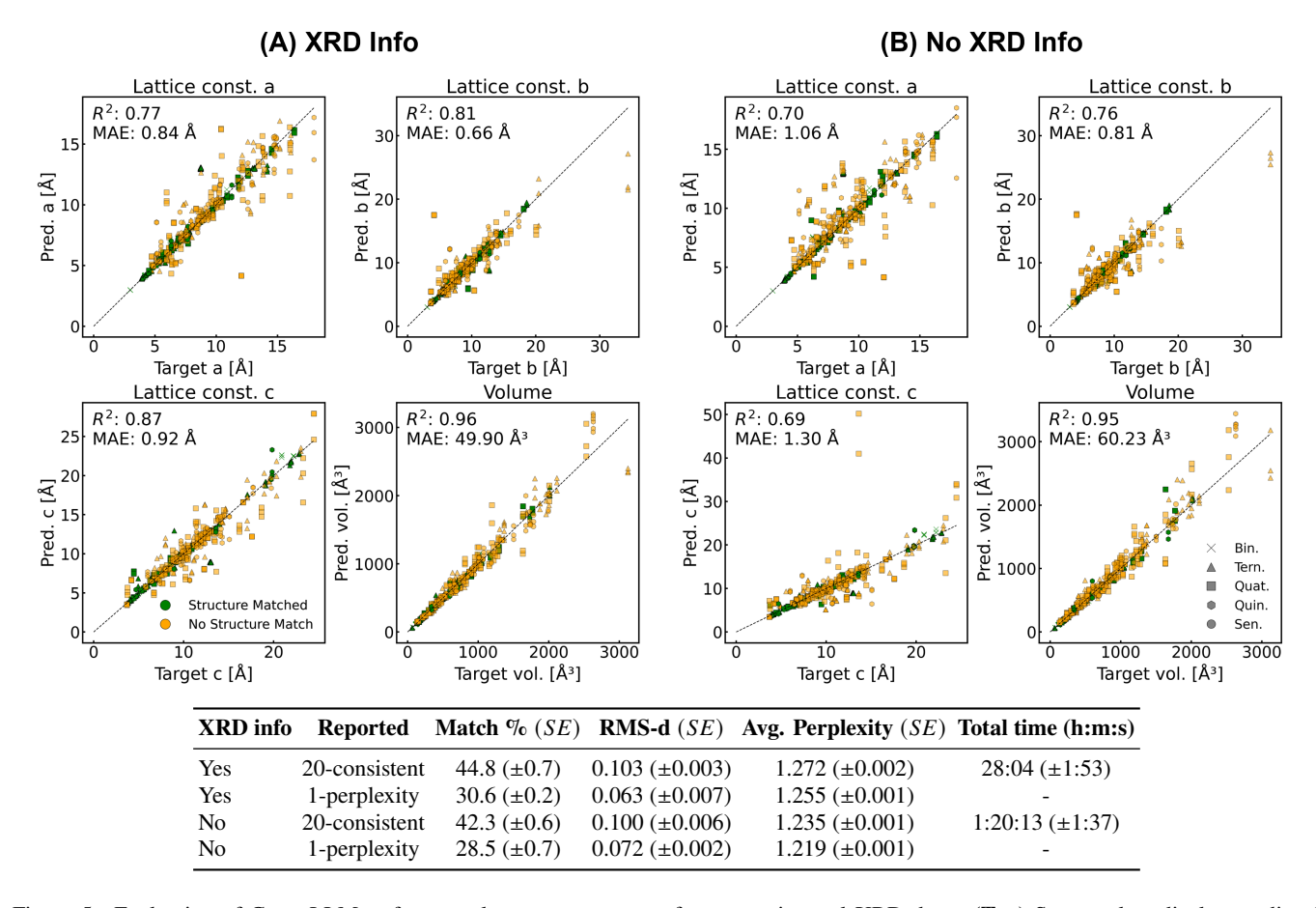


Figure 5. Evaluation of CrystaLLM- π for crystal structure recovery from experimental XRD data. (**Top**) Scatter plots display predicted (from generated structures) versus true (experimental structure) lattice parameters (a, b, c) and cell volume. The analysis compares model performance when conditioned with XRD data during generation (**A**) versus without conditioning (**B**). Marker colour distinguishes between matched structures (*green*) and non-matched (*orange*). Marker style informs on system complexity of experimental structures, ranging from binary to senary. The plotted points represent the best-matching structure from '20-consistent' generation attempts, with results aggregated from three identical and independent experiment repeats. (**Bottom**) Quantitative performance metrics are compared for models with and without XRD conditioning. Performance is assessed for both the '1-perplexity' metric and '20-consistent' generation attempts. Additionally, the computational time required to generate '20-consistent' structures for the 198 materials in the test set is reported, with an inference batch size of 20. All results are averaged over three identical and independent experiments to ensure robustness and report associated standard errors.

VSUN specs.	N Materials
Fine-tune, Structural	16463
Fine-tune, Compositional	15462
Pre-train, Structural	8712
Pre-train, Compositional	1809

Table IV. Number of Valid, Stable, Unique and Novel Materials dependent on novelty type and reference dataset (See Methods IV E). The matches are reported for 100K generations. The fine-tune dataset is MP SLME with 5.3K structures and the pre-train dataset is Le-Material with 4M structures. Structural novelty means there are no matching structures using pymatgen's StructureMatcher, and Compositional novelty indicates no structures with the same reduced formulas are in the reference dataset.

steer the model toward high-performance regions of chemical space. In this case as all data labels are homogeneous in

length and we have a sufficiently large set, we use the Prefix conditioning, to achieve a harder conditioning.

Table IV details how many Valid, Stable, Unique, and Novel (VSUN) structures were generated. A significant volume of high-quality candidates were generated, with a notable distinction in novelty profiles. Compositional novelty (no matching reduced formulas) with respect to the pre-training corpus is naturally lower (1,809 materials) than with respect to the smaller fine-tuning corpus (15,462 materials). This indicates effective knowledge retrieval as the model applies structural priors learned from millions of unlabeled crystals to the specific, data-scarce problem of photovoltaics. The 1,809 VSUN structures that are compositionally novel against the pre-training corpus demonstrate that the model generates candidates completely outside its training distribution.

The physical validity of the generated chemical space is analysed in Figure 6a. According to the detailed balance limit[60],

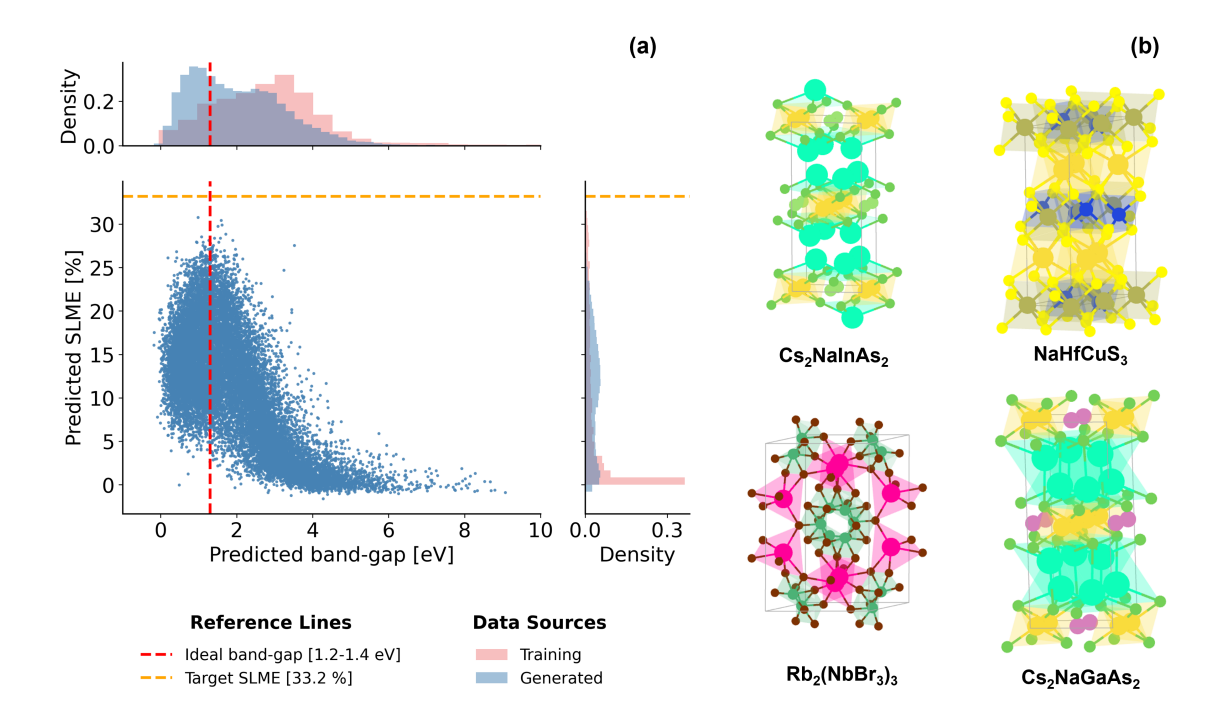


Figure 6. Exploration of the photovoltaic candidate chemical space. **a**, Scatter plot of surrogate SLME values against surrogate HSE06 band gaps for generated structures. The distribution highlights the model's implicit focus on the Shockley-Queisser optimal band gap range (1.2–1.4 eV), despite the absence of explicit band gap supervision. **b**, Crystal structures of four promising candidates validated with DFT. Cs₂NaInAs₂ (SLME: 26.4%, $E_{\text{hull}}^{\text{PBE}}$: $-0.605\,\text{eV/atom}$) and Cs₂NaGaAs₂ (SLME: 24.4%, $E_{\text{hull}}^{\text{PBE}}$: $-0.589\,\text{eV/atom}$) demonstrate successful retrieval of high-performance motifs seen during pre-training. NaHfCuS₃ (SLME: 23.3%, $E_{\text{hull}}^{\text{PBE}}$: $-0.013\,\text{eV/atom}$) is identified as a stable candidate and relatively sustainable. Rb₂(NbBr₃)₃ (SLME: 13.3%, $E_{\text{hull}}^{\text{PBE}}$: $0.001\,\text{eV/atom}$) was not seen in any training phase. Rb₂(NbCl₃)₃ structures (SLME: 11.6% and 11.3%, both $E_{\text{hull}}^{\text{PBE}}$: $0.003\,\text{eV/atom}$, 2 polymorphs not shown) were also identified as stable, promising candidates.

maximum efficiency for a single-junction device requires a band gap between 1.2 and $1.4\,eV$. Despite never receiving explicit band gap supervision during fine-tuning, the model's generated structures cluster near this optimal energy range, suggesting the model successfully learned an implicit mapping. By optimising for SLME, it converged on the specific structural motifs and bonding environments that give rise to optimal electronic structures.

A threshold of > 20% is considered indicative of a high-SLME material by the original Yu and Zunger paper[61]. Within the set of structurally novel materials shown in Table IV (VSUN Pre-train, Structural), the model generated 1,546 candidates with ALIGNN-predicted SLMEs above this threshold. While comprehensive characterisation of this extensive pool remains an opportunity for future work, here we focused on a representative subset of 30 top-ranking candidates selected based on ALIGNN predicted SLME and sustainability metrics (HHI, see Methods IV E). The rationale for selecting the specifically chosen candidates is outlined in Table XII. These were analysed before high-fidelity DFT was performed to verify the most promising entries. Figure 6b highlights four representative candidates.

The model employs chemically intuitive strategies for optimisation, such as atomic substitution on known high-performance

For example, the generation of Cs₂NaInAs₂ and Cs₂NaGaAs₂ leverages the known optoelectronic properties of InAs and GaAs motifs[63, 64] to propose stable quaternary variants, with high SLMEs. The model identified a metastable family of rubidium-niobium halides which are compositionally novel with respect to MP-SLME set. This group includes Rb₂(NbBr₃)₃ ($E_{\text{hull}}^{\text{PBE}} = 0.001 \, eV/\text{atom}$) and two structural polymorphs of $Rb_2(NbCl_3)_3$ ($E_{hull}^{PBE} = 0.003 \, eV/atom$ for both polymorphs). The Bromine candidate was completely unseen in any training phase (absent from LeMaterial and MP SLME). These materials have a band gap of around 1.6 eV, initially suggesting that they are promising PV materials. However, hybrid DFT reveals that the conduction band miniumum is split off from the main conduction band density of states, resulting in poor absorption properties and potentially low electron conductivity. The final generated material that we performed hybrid DFT on was NaHfCuS₃, here CrystaLLM- π proposes a chalcogenide variant, a class of materials known for applications in thin-film solar cells for example [65, 66], with a promising SLME of 22.6%. This material was not present in the fine tuning data, although it was present in the pre-training data. However, to the best of our knowledge, this material has never been investigated as a photovoltaic; this highlights the utility of CrystaLLM- π to uncover new potential applications for previously known but under-explored materials. We note

also that in Table XII the model has generated numerous low-HHI, high-SLME materials which we did not investigate further as they are already the focus of other PV research. While these materials may not be completely new for PV research purposes, their presence in the generated outputs reinforces the claim of CrystaLLM- π to be capable of generating viable functional materials given a specific set of conditions.

III. DISCUSSION

CrystaLLM- π is a framework for conditional crystal generation, by developing two novel conditioning mechanisms: Property-Key-Value (PKV) Prefix attention and the PKV Residual attention. By directly integrating continuous property information into the self-attention layers, the inefficient and syntactically disruptive tokenisation of numerical values is bypassed, enabling a more direct and efficient mapping between functional properties and crystallographic information. The efficacy of modifying the attention mechanism, as opposed to sequence-level conditioning, is demonstrated by more pronounced conditioning capabilities or a stronger ability to retain knowledge from large-scale pre-training. Studies in Section II C 1 show that the Prefix and Residual mechanisms clearly preserve the implicit understanding of chemical bonding and structural stability learned during pre-training, while steering generation toward a functional target. In contrast, baseline methods that alter the input sequence perturb learned representations more, leading to weaker pre-trained knowledge transfer and poorer generative performance.

The framework's flexibility was validated across two fundamentally different materials science challenges: novel material discovery and structure recovery. The model processed highdimensional X-ray diffraction (XRD) patterns to reconstruct crystal structures. When applied to experimental COD data, XRD-based conditioning clearly enhanced the accuracy of predicted unit cells and reduced the computation time to generate '20-consistent' structures by a factor of ~ 2.9 . This application demonstrated the framework's architectural flexibility, processing heterogeneous experimental data and allowing dynamic addition or removal of conditioning or symmetry constraints without pipeline modification. Furthermore, the model demonstrated efficient knowledge transfer after fine-tuning on a small dataset (~5.3K materials). When tasked with generating photovoltaic candidates with high Spectroscopic Limited Maximum Efficiency (SLME), the model implicitly learned to target the optimal $\sim 1.2 - 1.4 \, eV$ gap region without explicit band gap data. This indicates that the model can capture complex, multi-component structure-property relationships.

The framework offers a unified, computationally efficient architecture. Its lightweight 26-62M parameter models are substantially more accessible than large-scale autoregressive models, such as Uni3Dar (90M base parameters, but requiring an estimated 300-350M parameters from given model hyperparameters for the benchmarked XRD task in Section IID1), or general-purpose LLMs like DiffractGPT (7.3B parameters)[40, 55, 67]. This architecture contrasts with spe-

cialised, multi-component pipelines like PXRDGen, which integrates contrastive learning with CNN/Transformer, diffusion and structure refinement modules[56]. This unified design natively supports diverse generation modes on human-readable CIFs, capabilities often absent or requiring specialised variants in multi-component pipelines[20, 56].

Despite its flexibility, the framework is subject to a number of limitations. Firstly, while the model demonstrates generality across diverse properties, its performance remains bound by the underlying training data distribution. Studies show that neural networks exhibit greater stability to perturbations and better generalisation near the training data manifold compared to unexplored regions[68]. This suggests that generative success relies on the presence of materials in the training set which exhibit structural and physical properties near the target of interest. This is illustrated by the TiO₂ polymorph challenge, where the model's prior (eg. seeing only one polymorph for that cell composition) dominated the generative process, suggesting generative success depends on population density near the desired target space. Secondly, the model prioritises learned structural and cell composition constraints over property targets, particularly when a prompt strongly implies a single known structure. This suggests a tension between learned priors and external conditioning, potentially related to recency bias[69]. Finally, the implementation is constrained by the GPT-2 context length (which at 1024 limits the number of atoms per cell to ~ 20), a training corpus limited to ideal, ordered crystals and the need for robust postgeneration validation, unlike diffusion architectures that can incorporate certain physical constraints directly to the generative process[20, 30, 70].

These limitations define clear future research directions. Scaling the backbone architecture and positional encoding schemes[71, 72] would permit generation of larger structures, facilitated by a text-based representation which scales favorably compared to graph-based. Fine-tuning on datasets with partial occupancies could extend capabilities to disordered systems, which is natively supported by the CIF format. The model-agnostic nature of the Prefix and Residual mechanisms allows for broad applicability to other transformer-based models, whether in materials science or other fields. Further investigation into the mechanistic interpretability of the attention layers could elucidate the conditioning process, potentially allowing for boosted conditioning capabilities[73–75]. CrystaLLM- π thus provides an accessible and flexible framework for inverse materials design, engineering a direct pathway between continuous functional properties and autoregressive crystal structure generation.

IV. METHODS

A. Datasets

Datasets were curated to study the model under different pretraining and fine-tuning conditions as shown in Table V. All datasets were stored in dataframes, with each row containing a material's database of origin, its reduced formula, its augmented CIF string, and optionally numerical properties of interest along with their normalised counterparts. All the CIF data underwent a standardised preprocessing pipeline including deduplication, data augmentation, tokenisation and specialised batching to incorporate conditioning information, with full details provided in Appendix V B.For specific use cases we applied different pre-processing, full details for exact reproducibility can be found in Appendix V A.

Dataset	Nb Materials	Conditions
LeMaterial	4.35M	None
MP Bandgap	53.3K	Band gap, $E_{\text{bull}}^{\text{PBE}}$
MatterGen Density	653K	Band gap, $E_{\text{hull}}^{\text{PBE}}$ Density, $E_{\text{hull}}^{\text{PBE}}$
MP SLME	5.35K	SLME
MP-20 XRD	45.2K	Top-20 XRD
JarvisDFT XRD	76.0K	Top-20 XRD
MatterGen XRD	658K	Top-20 XRD
COD XRD	1.58K	Top-20 XRD

Table V. Summary of datasets used in this work. LeMaterial was the dataset used for large scale pretraining, and the rest were used in various conditional generation studies. Top 20 most intense peak intensities with their associated 2θ positions are stored for the X-Ray Diffraction (XRD) condition vector. Apart from the LeMaterial Dataset, all others were filtered to remove CIFs containing more than 1024 (context length) tokens. All processed datasets are available in open source on Hugging Face

B. Transformer backbone

In the pre-training phase, the model learns to generate CIFs sequentially. The model backbone is based off CrystaLLMs small model hyperparameter choices, and was pre-trained on an unlabeled augmented CIF dataset[48]. It consists of ~ 26 million parameters, with an embedding size of 512, 8 decoder block layers, and 8 attention heads. For functional property conditioning, the pre-trained model was adapted for fine-tuning. This stage utilised CIFs labeled with associated properties, such as band gap or density. Architectural modifications, detailed in Section IIB, were implemented to guide CIF sequence generation using these properties. The objective of this fine-tuning stage was to enable the model to learn a mapping from a vector of material properties to chemically valid crystal structures. Default model training protocols and hyperparameter choices can be found in Appendix VJ and the hyperparameter search space is defined for each experiment in Appendix V K. The final model configuration for every model used in this work can be found in the repository configuration files.

The model backbone was trained by minimising a developed variation of the cross-entropy loss, where the commonly used base loss is defined as:

$$\mathcal{L}_{CE} = \frac{1}{N} \sum_{n=1}^{N} \left(-\sum_{k=1}^{K} y_{k,n} \log(p_{k,n}) \right)$$
 (4)

where N is the total number of tokens in the batch for which the loss is calculated, K is the size of the token vocabulary, $y_{k,n}$ is the true probability for token k at position n in the sequence, set to 1 for the correct target token and 0 otherwise, $p_{k,n}$ is the model's predicted probability for token k at position n, and log is the natural logarithm.

The modification incorporates an additional penalty targeting *fixed* tokens. These tokens are defined as the syntactically invariable elements within the CIF (e.g., 'data_', '_cell_volume', see Appendix V C). Conversely, *variable* tokens are the parts of the CIF that can change from one structure to another (e.g. 'Ge4'), which are encapsulated in brackets during CIF augmentation. The penalty on *fixed* tokens aims to accelerate the learning of CIF syntax during initial training phases, diminishing gradually beyond the initial training phases as the models syntactic understanding improves. The final loss objective is defined as:

$$\mathcal{L} = n_1 \mathcal{L}_{CE} + n_2 \mathcal{L}_{Fixed}$$
 (5)

Where \mathcal{L}_{CE} is the regular cross-entropy loss and \mathcal{L}_{Fixed} is the additional cross entropy loss applied only to Fixed tokens. n_1 and n_2 are tuneable hyperparameters to adjust how much each component contributes to the overall loss \mathcal{L} . For the large scale pre-training, we set $\{n_1, n_2\}$ to $\{1, 2\}$, for the rest of the studies, we set them to $\{1, 1\}$.

C. Conditioning Method Implementation

To facilitate property conditioned generation, we set up a dual optimisation strategy during fine-tuning, adapting the AdamW optimiser inspired by Howard and Rude's recommendations[76, 77]. The parameter set of the model, θ , was split into two subsets: $\theta_{backbone}$ which contains the parameters of the pre-trained backbone and θ_{cond} which contains the parameters of the newly initialised conditioning layers. This partitioning allows for differential learning rates, with the goal of maximising the information transfer between pre-training and fine-tuning steps while enabling stronger learning of the conditioning task.

The full hyperparameter settings like hidden dimensions, dropout and the differential learning rates applied to $\theta_{backbone}$ and θ_{cond} for fine-tuning are provided in Appendix V J. Experiment specific hyperparameters are specified in the repository configuration files.

D. CIF generation and top perplexity scoring

During model inference, sampling is used to generate tokens sequentially. This work applies sampling temperature T, as well as Top-K and nucleus Top-p sampling schemes to allow dynamic selection of tokens[78, 79]. Tuning them allows sampling from highly likely tokens (reflecting frequent training patterns) to less likely tokens which introduces exploratory randomness during generation. The exact parameter values differ from experiment to experiment (See Appendix V G).

For crystal structure generation, text prompt and condition pairs are established, with specified levels of verbosity in the prompts. With the Residual method for example, we can include any combination of the following: functional property, no cell composition, cell composition, or space-group without needing to retrain the model or repurpose the framework. For each prompt-condition pair, the model generates candidate CIF structures using the specified sampling parameters.

A specific workflow was employed for structure recovery tasks to enhance prediction fidelity. For CIFs generated in Section II D, outputs underwent three consistency checks using algorithmic validation functions. Formula consistency verifies that the chemical formula is of coherent stoichiometry throughout the output CIF. Space-group consistency compares the stated space-group symbol in the output against the space-group detected by pymatgen's symmetry analysis with a precision tolerance of $0.1\,^{^{\circ}}A[80]$, confirming that the declared symmetry operations match the actual atomic arrangements. Sensibility tests apply physical constraints to unit cell parameters, rejecting structures with cell lengths outside $0.5-1000\,^{^{\circ}}A$ or cell angles outside $10^{\circ}-170^{\circ}$, filtering out geometrically unreasonable crystal structures. These self-consistency checks are performed to ensure basic chemical validity of proposed structures

To ensure quality, we employ perplexity-based scoring. In this case, the model computes the perplexity metric for generated tokens from their transition scores (excluding the input prompt). Lower perplexity values (close to 1) indicate higher model confidence in the generated sequence according to its learned probability distribution. For each prompt, we continue generation attempts until obtaining '20-consistent' CIFs, then rank all candidates by their perplexity scores. The '1-perplexity' scoring method selects the output structure with the lowest perplexity to put forward for structure matching. This approach balances exploration through sampling with quality control through validation and probabilistic ranking, increasing the models capacity to generate sensible structures for a given input (See Appendix V I for ablations).

E. Evaluation Metrics

To evaluate the developed methods, performance metrics used are CIF validity criteria for chemical consistency and structural reconstruction, structure similarity measures for novelty assessment against training data, uniqueness within generated sets, and statistics for comparative effectiveness of conditioning methods. DFT calculations then provide additional validation of thermodynamic stability and electronic properties for selected candidates.

1. Validity Criteria

The validity metric follows the original CrystaLLM paper's criteria[48]. It must be possible for a structure to be reconstructed from the generated CIF, the space-group must be con-

sistent with the atomic structure, the generated bond lengths must be reasonable with respect to the atomic radii, and finally the declared atom site multiplicity needs to be consistent with the unit cell composition.

2. Structure Diversity

For the uniqueness metric, sets of generated structures with identical input constraints are compared. We use LeMaterials BAWLHasher (Bonding Algorithm Weisfeiler Lehman), which is a materials fingerprint method based on bonding graph structure, reduced formula, and symmetry [45]. Canonical hashes are obtained for each structure in a uniqueness pass, and structures are counted as unique if they have a unique hash. This allows the calculation to scale O(n), rather than $O(n^2)$ when using a structure matcher algorithm for all generated materials.

To determine novelty, we compare unique generated structures against all training set structures with the same reduced formula. If a structures reduced formula does not appear in the reference dataset, it is considered *Compositionally* novel, if a generated structure shares a reduced formula with a reference one but the chemical structures do not match, it is considered *Structurally* novel. This matcher does not determine the general novelty of a material, but serves as a basic screening tool.

Pymatgen's StructureMatcher is used to match two chemical structures together. Unless otherwise specified, the default matcher settings are used, namely a fractional length tolerance of 0.2, a site tolerance of 0.3 Å, and an angle tolerance of 5°. For normalisation purposes, structures are reduced to their primitive cell and scaled to equivalent volume before matching.

3. Prediction models and DFT validation

High-throughput property estimation for generated structures was achieved using surrogate models based on the ALIGNN architecture[81]. In Section II C 1, PBE band gaps[82] were predicted using the standard 'mp_gappbe_alignn' model trained on Materials Project data. For the specific requirements of Section II E, we trained distinct surrogate models to predict higher-fidelity properties. HSE06 band gaps[83] were predicted using an ALIGNN model trained on $\sim 10 k$ labeled structures from Kim et al.[84], with hyperparameters according to Choudhary et al.[81] SLMEs were predicted using a model trained on the $\sim 5.3 k$ entry MP-SLME dataset[62].

The thermodynamic stability of generated materials was first evaluated using the MACE-MP calculator to determine the energy above the convex hull, denoted here as $E_{\rm hull}^{\rm MACE}$. MACE-MP is a graph-based foundation model employing higher-order equivariant message passing, pre-trained on MP relaxation trajectories[85]. Predicted energies were processed using the MaterialsProject2020Compatibility scheme to ensure

consistency between GGA and GGA+U calculations relative to the MP dataset.

Given the model's reported mean absolute error (MAE) of $0.057\,eV/{\rm atom}$ on the Matbench Discovery benchmark[86], stability thresholds were adjusted to account for statistical uncertainty. For the general validation in Section II C 1, a threshold of $E_{\rm hull}^{\rm MACE} \leq 0.157\,eV/{\rm atom}$ was employed, expanding upon the typical $0.1\,eV/{\rm atom}$ metastability limit[57]. Conversely, for the SLME Study in Section II E, a stricter threshold of $E_{\rm hull}^{\rm MACE} \leq 0.1\,eV/{\rm atom}$ was applied to aggressively funnel the discovery pipeline. The final VSUN metric integrates this stability assessment with checks for Validity, Uniqueness, and Novelty[30].

To validate the stability of promising candidates identified in the SLME study, structure optimisation and energy calculations were performed at the Density Functional Theory (DFT) level to obtain $E_{\rm hull}^{\rm PBE}$. We used the Vienna *ab initio* Simulation Package (VASP)[87, 88], employing PBE exchange-correlation functionals and Projected Augmented Wave (PAW) potentials[89, 90] matching MP v54 selections. The relaxation protocol involved sequential optimisation of ion positions and lattice parameters, followed by a final refinement step to ensure convergence within standard MP thresholds. Total energies were derived from a final static calculation with a dense k-point mesh, ensuring energetic consistency with reference compounds for convex hull analysis. All relaxations were performed without symmetry constraints.

Detailed optical properties were subsequently computed for verified structures using a hybrid functional workflow. Following a PBE relaxation, frequency-dependent dielectric functions were calculated using the HSE06 functional[83] within the Independent Phase Approximation (IPA). Input files were generated using Atomate2[91], but for the final dielectric calculations k-point meshes were made twice as dense as those generated by Atomate2 in each reciprocal space direction to ensure convergence of optical properties. This produced a mesh with $\sim 2000/n$ k-points for a unit cell with n atoms. Dielectric functions were converted to absorption spectra using Kramers-Kronig transformations and used to determine the SLME following the method of Yu and Zunger[61] for an absorber at 300 K and with thickness d = 500 nm as is widely used[61, 92].

Supply chain sustainability was evaluated using the Herfindahl-Hirschman Index (HHI) for elemental production (HHI_P) and reserves (HHI_R) , based on data from Gaultois et al.[93] Material-level scores were computed as the massfraction weighted average of the constituent elements' HHI values extracted with SMACT[94]. To prioritise candidates with diverse and secure global supply chains, we employed a composite sustainability metric defined by the Euclidean distance from the origin in the HHI space:

$$HHI_{dist} = \sqrt{HHI_P^2 + HHI_R^2} \tag{6}$$

A lower HHI_{dist} corresponds to reduced geopolitical influence and higher supply security, serving as a selection criterion for the final candidate pool.

4. Performance Comparison for Conditional Models

When a model is evaluated on its capability to generate materials with targeted properties, different evaluation metrics are used for comparative analysis. Common statistical metrics, which include the Mean Average Error (MAE), standard error (SE), Pearson's r (r), correlation coefficient (R^2) and the dependent t-test for paired samples (t,p), are not reiterated here. The Hit-Rate is defined in this work as the number of materials that have a predicted property that fall within a specified range of the target value, and it is determined as:

Hit – Rate_{\varepsilon} =
$$\frac{1}{N} \sum_{i=1}^{N} (|\hat{y}_i - y_i| \le \varepsilon)$$
 (7)

where default $\varepsilon = 0.5 \, eV$ (used for Section II C 1).

F. Code and Data Availability

The code for CrystaLLM- π is available at the model repository (to be made public soon), which includes a detailed README.md on how to load and generate structures with the models mentioned in this work, as well as how to adapt the framework for other use cases. Importantly, the Prefix attention method is called 'PKV' in the repository, and the Residual attention method is defined as 'Slider' in the repository. Processed datasets and trained models used in this work are stored on Hugging Face. Data preparation, training, and metric calculation workflows are all detailed in the repository notebooks. Exact training and generation hyperparameters for every experiment carried out in this work can be found in the repository configuration files.

G. Acknowledgements

KTB acknowledges funding from EPSRC (EP/Y014405/1, EP/Y000552/1, EP/Y028775/1 and EP/Y028759/1). We acknowledge the use of UCL Myriad High Performance Computing Facility (Myriad@UCL), and associated support services, in the completion of this work. We acknowledge Young HPC access which is partially funded by EPSRC (EP/T022213/1, EP/W032260/1 and EP/P020194/1). CB and MW are funded by a UCL start-up package. Part of this publication is based upon work from EUMINE COST Action CA21143, for the STMS supported by COST (European Cooperation in Science and Technology). KL is supported by the Bezos Earth Fund via the Earth Rover Program (G-2023-201305339).

H. Author Contributions

CB and KTB conceptualised the project and wrote the initial manuscript, the package was developed by CB as a development from the CrystaLLM code written by LA, the Residual model was based off code provided by KL. Experimental XRD

data was provided by AA and JD. DFT calculations and FGW distance evaluations were performed by MW. RG-C, LA and KL provided feedback and guidance on project design and were also involved in editing the final manuscript.

I. Competing Interests

The authors declare no competing interests.

V. APPENDICES

A. Property-labeled Dataset Construction Details

The LeMaterial dataset does not contain any functional properties, it is exclusively made up of unlabeled CIFs derived from the source material [45], randomly split into a train:validation ratio of 90:10.

For property-labeled datasets, we firstly consider the MatterGen Alex-MP-20 data[30], accessed April 2025. Structures have at most 20 atoms per unit cell and an $E_{\rm hull}^{\rm PBE}$ of at most $0.1eV/{\rm atom}$. All structures are relaxed with DFT using a PBE functional with corrections based on the Materials Project[57] for energy consistency. All Mattergen datasets were randomly split into train:validation sets with a 90:10 ratio. The **MatterGen Density Subset** considered for the porous silicate study was curated by calculating density using pymatgen's Structure.density in $(g/{\rm cm}^3)$. $E_{\rm hull}^{\rm PBE}$ values were taken directly from the base dataset. Density and $E_{\rm hull}^{\rm PBE}$ were normalised using Min-Max method. To generate XRD spectra for conditioning vector in **MatterGen XRD** dataset, XRD patterns were calculated with Pymatgens XRDCalculator at the CuK α wavelength. The 20 most intense Bragg peaks and their 2θ positions were stored. The intensities and 2θ values were normalised with Min-Max normalisation where 0:90 for 2θ and 0:100 were used for min-max ranges. Patterns with under 20 Bragg peaks were padded with [-100] tokens, indicating a heterogeneous 'missing value'.

The Materials Project API was queried to to make the **MP Bandgap** dataset [57], accessed in April 2025. All structures are relaxed with DFT using a PBE functional with the Materials Project corrections. Band gaps and $E_{\text{hull}}^{\text{PBE}}$ were retrieved directly from the API. Materials with null band gaps were removed. The database was randomly split into train:validation sets of 90:10 ratio.

The MP-SLME dataset was curated from Walker and Butler's dataset, accessed in September 2025[62], created by taking overlapping materials from the Woods-Robinson et al. and Kim et al. datasets[84, 95]. The Spectroscopic Limited Maximum Efficiency (SLME) values were derived from high fidelity absorption spectra and band gaps were calculated with the Heyd-Scuseria-Ernzerhof (HSE) hybrid DFT functional. CIFs were then obtained from Materials Project IDs associated to each property value. For hyperparameter search, the dataset was split into 95:5 train:validation ratio, but for the final model the full dataset was put into the training set.

The MP-20 dataset was used to curate the **MP-20 XRD** dataset. The structures are a subset of the materials project material with at most 20 atoms per unit cell. The XRD conditioning property vectors were generated with the same methodology as the **MatterGen XRD Subset**. The dataset was split into train:validation:test sets of 60:20:20 with the material splits taken directly from PXRDGen[56].

The Jarvis-DFT dataset[58] was used to curate the **JarvisDFT XRD** fine-tuning subset, accessed in January 2025. All structures are relaxed with DFT using a PBE functional. The XRD conditioning property vectors were generated with the same methodology as the **MatterGen XRD Subset**. The database was randomly split into train:validation:test sets of 80:10:10 for hyperparameter search, and then 90:10 train:test for the final model to match the benchmark.

The **COD XRD** dataset was curated from the Crystallographic Open Database (COD)[96], accessed in June 2025. We filtered the data down to exclusively inorganic materials by removing all hydrocarbon containing compounds. Structures with partial atomic site occupancies were processed to approximate corresponding fully ordered crystals. Site occupancies deviating by less than 5% from an integer or simple fraction were rounded, while structures with larger deviations were discarded. Doped materials were also removed. For each material, an XRD conditioning vector was generated from experimental (h, k, l) Miller indices stored in the database and associated intensities. The diffraction angle, 2θ , for each peak was calculated from the crystal's lattice parameters. First, the interplanar spacing, d_{hkl} , for an experimentally observed (h, k, l) plane was determined using Pymatgen's structure.lattice.d_hkl([h, k, 1]). Then, the Bragg angle θ was calculated by rearranging Bragg's Law,

$$\lambda = 2d_{hkl}\sin(\theta_{rad}) \tag{8}$$

where λ is the X-ray wavelength, specified as 1.5406 Å corresponding to a CuK α source to be consistent with the theoretical training data. The angle in radians was obtained using the inverse sine function,

$$\theta_{\text{rad}} = \arcsin\left(\frac{\lambda}{2d_{hkl}}\right) \tag{9}$$

and then converted to degrees to yield the final diffraction angle,

$$2\theta_{\text{deg}} = 2\theta_{\text{rad}} \cdot \frac{180}{\pi} \tag{10}$$

The 20 most intense peaks and associated and 2θ values were normalised with Min-Max normalisation, where we used 0:90 for 2θ and 0:100 for min-max ranges. Patterns with under 20 Bragg peaks were padded with [-100] tokens, indicating a 'missing value'. Finally, the resulting dataset was split randomly into training, validation and test sets with a 75:12.5:12.5 split.

B. Preprocessing and Batching

The base CrystaLLM- π model trains to learn patterns on a large corpus of CIFs. Before this, the relevant data needs to be preprocessed to an optimised machine readable format. In essence, preprocessing steps include CIF deduplication, augmentation, and tokenisation. They follow the same core logic as the original CrystaLLM work[48].

Deduplication was performed by keeping the lowest volume per formula unit structure for identical cell composition and space-group. For **data augmentation**, symmetry information was embedded using pymatgens symmetry finding with a tolerance of $0.1\,^{\circ}A$, and floating point numbers were all rounded to 4 decimal places. Additionally, brackets were added to the CIF, encapsulating parts that vary between crystal structures as described in Section IV B, like 'data_[Ge4]' where text inside the brackets is considered *variable*, and outside the brackets is considered *fixed*. For an example of a fully augmented CIF, see Figure V C.

For **batching**, sequences longer that context length were truncated, and shorter ones were stacked in a roundrobin manner until the length was reached, detailed in Pseudocode 1. The input sequences were allowed to contain multiple CIFs, however when conditioning only the first CIF's condition vector was applied. Training data was shuffled at each epoch during training, so CIF stacking was never twice the same during training.

Algorithm 1 Round-robin packing of CIF token sequences to context length C

```
Input: List of N token sequences \{X_0, X_1, \dots, X_{N-1}\} (Each X is a CIF in dataloader)
Output: Packed sequence out with length exactly C (context length)
 1:
 2: function ROUNDROBIN(features, C)
        for i \leftarrow 0 to N-1 do
 3:
            X \leftarrow \text{features}[i].X
 4:
 5:
            if len(X) \ge C then
                                                                                                                   ▶ CIF is longer than context, slice it
 6:
                out \leftarrow X[0:C]
 7:
                return out
 8:
            end if
 9.
10:
11:
            out \leftarrow X
                                                                                                                                ▶ Start with current CIF
            current\_index \leftarrow i
12:
13:
                                                                                                                 > Append more until context reached
14:
            while len(out) < C do
15:
                current\_index \leftarrow (current\_index + 1) \mod N
                                                                                                                                         ▶ Next in batch
                next\_CIF \leftarrow features[current\_index].X
16:
                remaining\_space \leftarrow C - len(out)
17:
                tokens\_to\_take \leftarrow min(len(next\_CIF), remaining\_space)
18:
                Append next_CIF[0:tokens_to_take] to out
19:
20:
            end while
21:
            out \leftarrow out[0:C]
                                                                                                                        > trim to exact length if needed
22:
            return out
23.
        end for
24.
25: end function
```

C. Augmented CIF

```
<bos>
data_[Ge4]
loop_
_atom_type_symbol
_atom_type_electronegativity
atom type radius
atom type ionic radius
Ge 2.0100 1.2500 0.7700
_symmetry_space_group_name_H-M [P6_3/mmc]
cell length a [4.0500]
cell length b [4.0500]
cell length c [6.6840]
_cell_angle_alpha [90.0000]
cell angle beta [90.0000]
_cell_angle_gamma [120.0000]
symmetry Int Tables number [194]
chemical formula structural [Ge]
chemical formula sum '[Ge4]'
_cell_volume [94.9443]
cell formula units Z [4]
loop
_symmetry_equiv_pos_site id
symmetry equiv pos as xyz
1 'x, y, z'
loop_
atom site type symbol
_atom_site_label
atom site symmetry multiplicity
atom site fract x
atom site fract y
atom site fract z
atom site occupancy
Ge Ge0 4 0.3333 0.6667 0.4371 1.0
1
<eos>
```

Figure 7. Example of an augmented CIF for Ge4. The *variable* tokens are set in red and *fixed* tokens are in black.

D. Baseline model comparison - challenge benchmark

Metrics	Crys	taLLM	CrystaLLM- π		
TVICTIES	No s.g.	With s.g.	No s.g.	With s.g.	
Success. Gen. Rate Matches (Seen) Matches (Unseen)	85.7% 50.0% 25.9%	88.6% 50.0% 34.5%	88.6% 50.0% 22.4%	88.6% 50.0% 30.4%	

Table VI. Performance comparison between the original CrystaLLM and the CrystaLLM- π backbone on the challenge benchmark from Antunes et al.[48] The metrics assess the model's ability to generate valid crystal structures from cell composition prompts, both with ('With s.g.') and without ('No s.g.') space-group information. A material is classified as 'unseen' if no compound with an identical cell composition and space-group was present in the training dataset. The minor differences in performance (within ± 4.5 percent points in every metric) are attributed to framework updates in the 2.0 version, including a transition to a Hugging Face GPT-2 architecture, pre-training on the expanded LeMaterial dataset (4.2M structures), and and changes in pre-processing and batching to incorporate conditioning information (See Appendix V B and Methods). The reported results for CrystaLLM- π encompass all 70 generation targets performance is enhanced for the 64 targets that fall within the model's 1024-token context limit.

E. Architectural details for Encoders

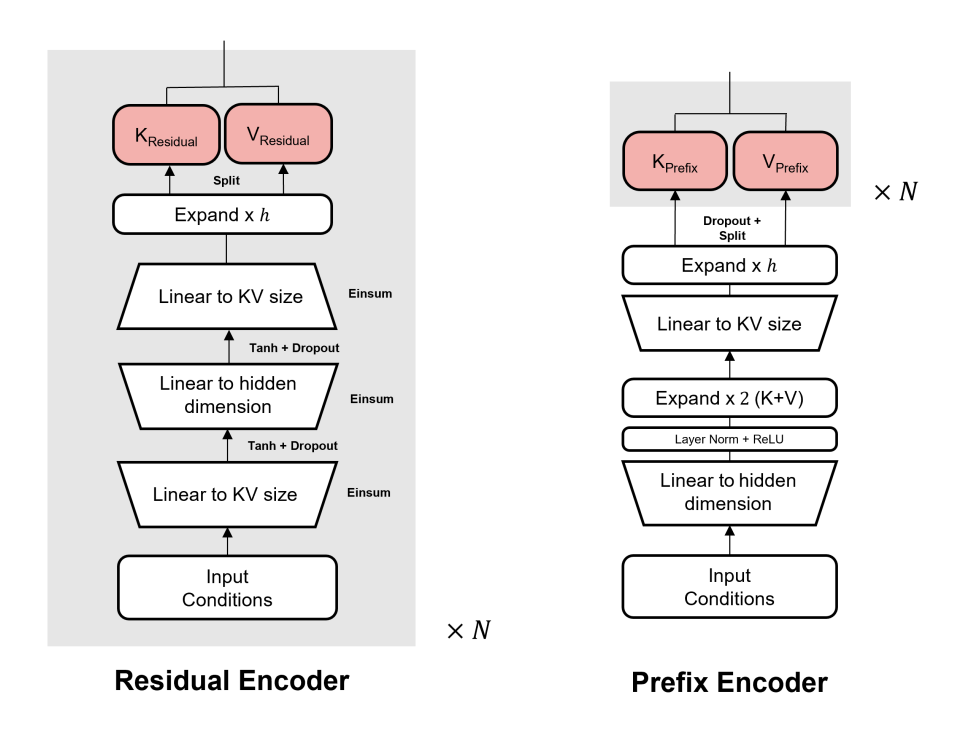


Figure 8. Residual and Prefix conditioning Encoders. Both take in a set of input conditions (property vector) and output a learned set of KV embeddings (one for each property) which matches the expected dimensions of the model's attention mechanism. The main difference between encoders is that the Residual Encoder uses Einstein summation (einsum) operations to ensure individual input properties influence different regions of the latent representation space, necessary so each property may have an associated KV pair. For the Prefix Encoder, the generated set KV pairs cannot be associated directly to individual properties.

F. Architectural details for PrependGPT

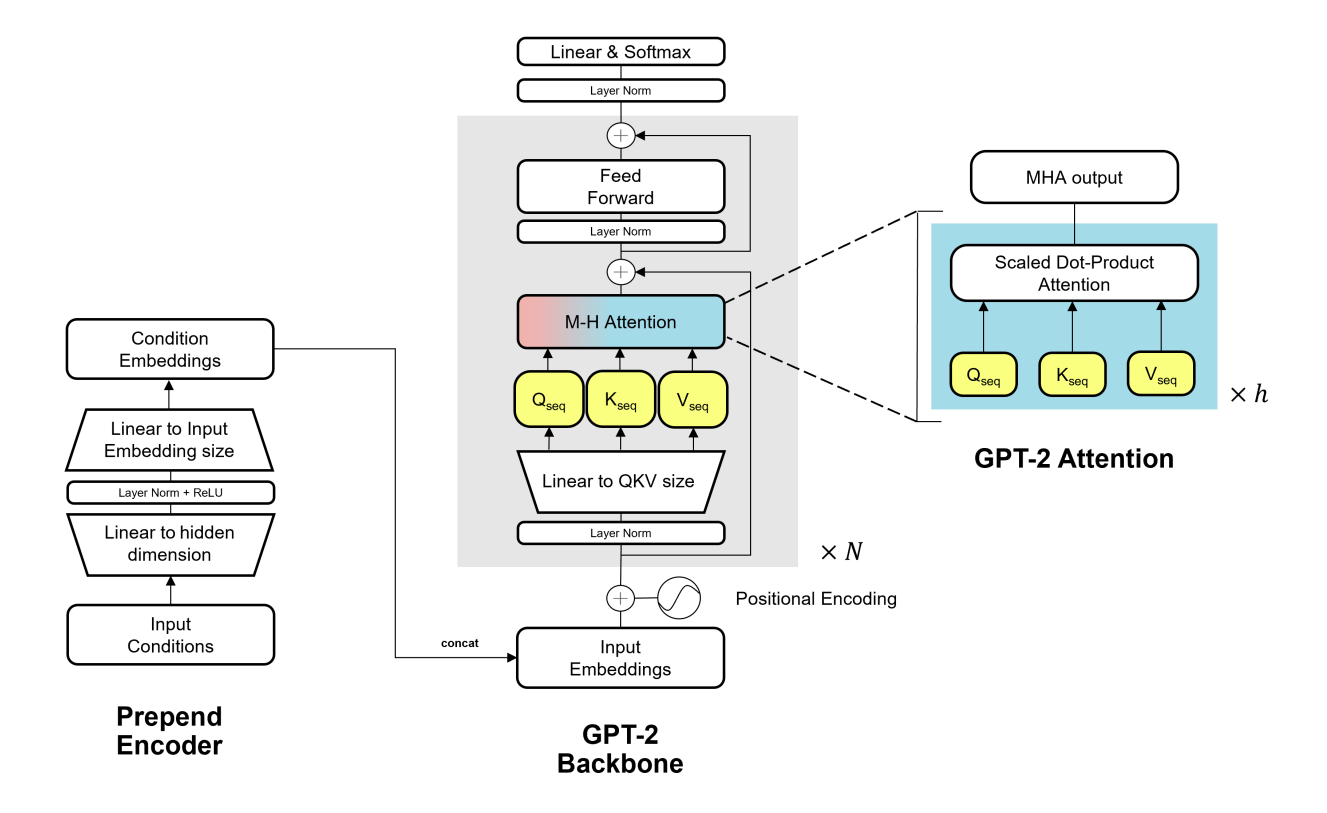


Figure 9. Prepend Conditioning method architecture. The Prepend Encoder handles the transformation of the condition vector into an embedding of the same size as the input sequence embeddings. The rest of the model behaves as per the backbone.

G. Experimental protocols

The challenge **benchmark study** was replicated with as much detail as possible to the original CrystaLLM paper[48]. The challenge set contains 70 structures, with 12 seen during general pre-training, and the rest obtained from recent literature. The dataset was filtered down to compounds within the hard token generation limit set by Hugging Face's implementation of GPT-2, resulting in 64 structures. We sampled the models to generate CIFs with T = 0.7, top-K = 10, top-p = 0.95 with 100 generation attempts per structure. For each structure, generations were carried out in one case with space-group information, and in another case with only cell composition information.

The MP Bandgap dataset was used to train the models for Section II C 1. All four conditioning methods were tested to evaluate their information retention capabilities and initially screen their conditioning abilities. Conditioning models were either trained from scratch on the dataset, or fine-tuned from the pre-trained model. We sampled each models at both regimes to generate CIFs with T = 0.7, top-K = 30, top-p = 0.95. The prompts were set to be ab-initio, so we did not specify a cell composition. For each trial, we prompted the model with 8 different conditions, to showcase how the model performs in areas of high and low training set density frequencies. These were $0.07, 0.18, 0.68, 1.55, 2.44, 3.72, 6.78, 12.1 \, eV$, but the number seen by the model was the normalised version of these. For each of the conditions, we also added $E_{hull} = 0$ as the second condition. We generated 1K structures for each of the conditions.

In Section II C 2, the Mattergen Density dataset was reduced to 1K, 10K, and 100K structures using random sampling as shown in Figure 10. For the 4 sets, pre-trained models were fine-tuned on each subsets and evaluated on conditional generation capabilities.

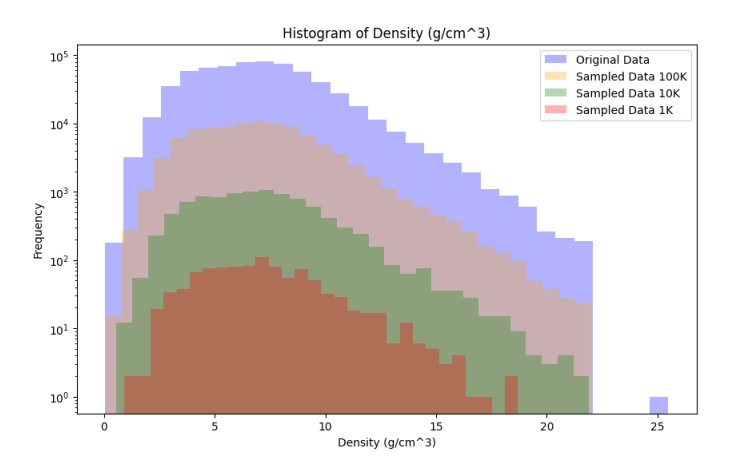


Figure 10. Visualisation of the density distribution of different randomly sampled subsets of data used in the dataset size study. As we go to lower subset sizes, we notice a decreasing spread of property values, meaning we not only have less data, but also less diversity of data.

We sampled the models to generate CIFs with K = 1.0, top-K = 15, top-P = 0.95. The prompts were set to be ab-initio, so we did not specify a cell composition. For each trial, we prompted the model with three different conditions, to showcase how the model performs in areas of high and low training set density frequencies. These were 1.27, 15.30, 22.94 g/cm³, but the number seen by the model was the normalised version of these. For each of the conditions, we also added $E_{\text{hull}} = 0$ as the second condition. We generated 1K structures for each of the conditions.

For the discovery task, the final MP-SLME dataset was used to fine-tune the base model to condition CIF generation on associated SLME percentages. We sampled the model to generate 100K CIFs with T = 1.0, top-K = 50, top-p = 0.95. The prompts were set to ab-initio, so we did not specify a cell composition. A higher top-K value was selected to expand the accessible chemical space during the sampling of atomic species. This approach prevents the model from being restricted to only the most common elements, thereby increasing the diversity of atomic types available for ab-initio material discovery.

For materials recovery tasks, we employed the various XRD related datasets. Because this task is more constrained (more conditions, heterogeneous data, additional cell composition and sometimes space-group information), we employed the '1-perplexity' sampling scheme for the crystal structure predictions, for which the effectiveness was validated in Appendix VI. T = 0.75, top-K = 10, top-p = 0.95 were chosen as the sampling parameters. The temperature parameter was picked by scanning across various temperature ranges and optimising match rates and RMS-d metrics on a sub-sampled test set for both '20-consistent' and '1-perplexity' scored CIFs (See Methods IV D for details on the sampling schemes, and Appendix V I for the ablation study). For all the studies, we prompted the model with cell composition plus XRD information. In the case of the polymorph recovery study (Section II D 2), adding space-group information was also evaluated, as well as prompting models with 2× the stoichiometry of their true cell composition, akin to a supercell.

H. Fine-tuning Losses

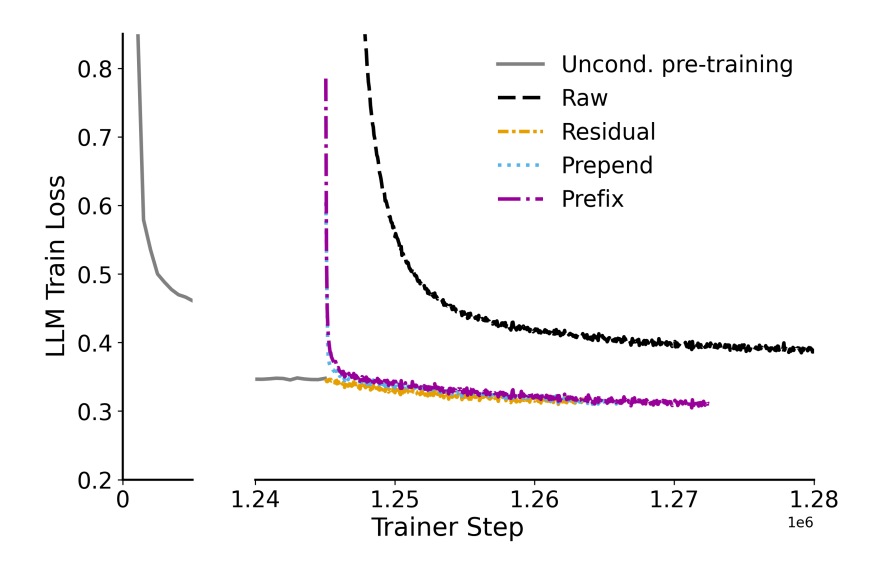


Figure 11. Evolution of training loss from pre-train to fine-tuning regimes depending on the conditioning method. The pre-training was run for 1.25 million steps, and fine-tuning was run for 50K steps with early stopping, each with the same hyperparameters.

I. Sampling Scheme Parameter Studies for Structure Recovery Tasks

To determine optimal hyperparameters and generation strategy for the crystal structure recovery tasks, a series of ablation studies were conducted on a 1K structure subset of the MP-20 test set.

The first study, shown in Table VII, gives a sampling temperature of T = 0.75 as a good balance between recovery accuracy and generative diversity. While a lower temperature of T = 0.5 yields a marginally better RMS distance, selecting T = 0.75 increases the 1-perplexity match rate by 1.4% points, maximising the probability of identifying the correct structure in a single closed loop attempt. Higher temperatures offered a slight increase in the match rate for 20-consistent CIF generation attempts but at the cost of reduced structural accuracy.

The second study, shown in Table VIII confirms the benefits of both XRD conditioning and perplexity-based ranking. Providing XRD information consistently improves both the 1-perplexity match rate (+3.3% points) and the RMS-d (-0.0058). Then, ranking candidates by perplexity provides an improvement again for both metrics without any trade-off.

Model	Temp	Ranking Scheme	Match Rate (%)	RMS-d	Avg. Perplexity
	0.5	20-consistent	73.2	0.0379	1.151
	0.75	20-consistent	75.3	0.0393	1.164
	1.0	20-consistent	76.4	0.0467	1.172
	1.25	20-consistent	76.3	0.0461	1.176
CrystaLLM-π	1.5	20-consistent	76.6	0.0532	1.181
	1.7	20-consistent	76.2	0.0580	1.181
	0.5	1-perplexity	63.6	0.0408	1.136
	0.75	1-perplexity	65.0	0.0465	1.148
	1.0	1-perplexity	63.2	0.0504	1.154
	1.25	1-perplexity	61.0	0.0473	1.154
	1.5	1-perplexity	58.4	0.0511	1.158
	1.7	1-perplexity	56.6	0.0511	1.156

Table VII. Ablation study for sampling temperature optimisation. The model was trained from scratch on the MP-20 XRD dataset. The 'N-consistent' means we generate until we reach N self-consistent CIFs (that pass basic chemical validity checks), and '1-perplexity' selects the output with the lowest perplexity score out of the N-consistent CIFs for matching, as described in Section IV D.

Model	Temp	Ranking Scheme	XRD Info	Match Rate (%)	RMS-d	Avg. Perplexity
	0.75	20-shot	No	73.8	0.0427	_
	0.75	20-shot	Yes	75.3	0.0418	_
CrystaLLM-π _	0.75	20-consistent	Yes	75.3	0.0393	1.164
Crystal 22 77	0.75	1-shot	No	59.5	0.0589	_
	0.75	1-shot	Yes	62.8	0.0531	_
	0.75	1-perplexity	Yes	65.0	0.0465	1.148

Table VIII. Ablation study on the utility of XRD conditioning and perplexity-based ranking. The model was trained from scratch on the MP-20 XRD dataset. 'N-shot' means we perform N generations and match against these, whereas 'N-consistent' means we generate until we reach N self-consistent CIFs (that pass basic chemical validity checks), and '1-perplexity' selects the output with the lowest perplexity score out of the N-consistent CIFs for matching, as described in Section IV D.

J. Default Hyperparameters for Pre-training and Framework Validation

The model backbone consists of 26 million parameters with an embedding size of 512, 8 decoder layers, and 8 attention heads, following CrystaLLM's small model architecture[48]. Training employed DeepSpeed Stage 2 optimisation across 2 NVIDIA L4 GPUs with early stopping based on validation loss plateau or increase to avoid overfitting. For the exact hyperparameter values used during training, see Table IX and configuration files are available in the project repository.

Unless hyperparameter searches were carried out, default training hyperparameters were used in the various studies of this work. For default pre-training on the structure only dataset, the model used cosine learning rate scheduling with the AdamW optimiser. Default conditional fine-tuning continued from pre-trained checkpoints with reduced learning rates for backbone parameters while newly initialised conditional encoders used higher learning rates. The conditional encoder hidden dimension was set to 1024 with reduced regularisation compared to pre-training.

Models trained from scratch in comparative studies used default fine-tuning hyperparameters with higher regularisation. Training duration varied by study design, with pre-training benefits experiments using 50K steps and dataset size studies scaling from 1.4K to 400K steps based on dataset size.

Hyperparameter	pre-training	fine-tuning
Optimiser	AdamW	AdamW
Learning Rate	10^{-3}	5×10^{-6}
LR Schedule	Cos. to 0.1%LR	Cos. to 1% LR
β_1	0.85	0.9
eta_2	0.98	0.999
Gradient Clipping	1.0	1.0
Batch Size	32	32
Dropout	0.1	0.1
Weight Decay	0.1	0.01
Context Length	1024	1024
Training Steps	1.250M	Varies
Warmup	0 steps	2% of steps
Cond. Hidden Dim.	_	1024
Cond. Dropout	_	0.01
Cond. LR	_	5×10^{-4}
Cond. Weight Decay	_	0.01

Table IX. Hyperparameter settings for pre-training and conditional fine-tuning steps: 50K (pre-training benefits), 1.4K-400K (dataset size study). From-scratch models used backbone LR 10^{-3} , conditional LR 10^{-3} , weight decay 0.1, and 15K steps. Cond. indicates values specific to the conditioning encoder. LR indicates the Learning Rate. Cos. indicates cosine annealed learning rate schedule to a target percent of the base learning rate.

K. Discovery and Recovery hyperparameters

For specialised conditional generation tasks, hyperparameter search was conducted using Optuna with MedianPruner across 50 trials[97]. Validation sets were created to guide the search by withholding 5% of data for SLME studies and 10% for COD and Jarvis datasets. Following hyperparameter optimisation, final training utilised the complete datasets with training steps scaled proportionally to account for the withheld data being put back into the training set. Early stopping was implemented to avoid overfitting during both search and final training phases. The hyperparameters not optimised here were set to the default values as specified in the previous section.

COD XRD employed two-stage fine-tuning, first training on MatterGen XRD data then COD-specific optimisation, resulting in substantially lower learning rate ranges (10^{-8} to 10^{-6}). MP-20 XRD scratch models were trained from scratch using learning rates optimised in the (10^{-5} to 10^{-2}) range. SLME and Jarvis XRD studies employed fine-tuning procedures with learning rates in the (10^{-7} to 10^{-5}) range for backbone parameters. The learning rates were consistently found by the hyperparameter search software to be the main impact on validation loss.

Train Dataset	Architecture	Train Phase	Val. Holdout	Trials	Optimised Parameters
MP SLME	Prefix	1	5%	50	Cond. Prefix Tokens: [1-5], Cond. Hidden Dim.: [512-1024] Base LR: $[5 \times 10^{-7} - 5 \times 10^{-5}]$ Cond. Dropout: [0.0-0.2], Warmup steps: [50-500] Weight Decay: [0.01-0.2], Cond. Weight Decay: [0.01-0.3]
MP-20 XRD	Residual	0	Existing	50	Base LR: $[1 \times 10^{-5} - 1 \times 10^{-2}]$ Cond. Dropout: [0.0-0.2], Warmup: [1-10%] Weight Decay: [0.01-0.2], Cond. Weight Decay: [0.01-0.3] Dropout: [0.0-0.2]
Jarvis XRD	Residual	1	10%	50	Base LR: $[5 \times 10^{-7}-5 \times 10^{-5}]$ Cond. LR: $[1 \times 10^{-4}-1 \times 10^{-3}]$ Warmup: $[1-10\%]$, Cond. Dropout: $[0.0-0.2]$ Weight decay: $[0.01-0.2]$, Cond. Weight Decay: $[0.01-0.3]$
COD XRD	Residual	2	10%	50	Base LR: $[5 \times 10^{-8} - 5 \times 10^{-6}]$ Cond. LR: $[5 \times 10^{-6} - 5 \times 10^{-4}]$ Warmup: $[1-10\%]$, Cond. Dropout: $[0.0-0.2]$ Weight decay: $[0.01-0.2]$, Cond. Weight Decay: $[0.01-0.3]$

Table X. Hyperparameter optimisation configurations for specialised conditional generation studies. All studies used MedianPruner with TPESampler. Training steps varied: SLME (16k), MP-20 scratch (30k), Jarvis (16k), COD (5k). COD XRD used two-stage fine-tuning: MatterGen XRD (500k steps) followed by COD-specific optimisation. Cond. indicates values specific to the conditioning encoder. LR indicates the Learning Rate. The Train. Phase indicates from where we pick up training, 0 is training from scratch, 1 is loading the base model pre-trained weights, and 2 means we are at a second fine-tuning pass.

L. Open Sourced Models

Model Name	Study	Availability	Model Parameters	Training Dataset	Method	Property Vector
CrystalLLM-π Base	II A	Open-Source	25.9M	LeMaterial	Base	None
CrystalLLM- π Band gap	IIC1	Open-Source	61.6M	MP Bandgap	Prefix	[Band gap, $E_{\rm hull}^{\rm PBE}$]
CrystalLLM- π Density	IIC2	Open-Source	61.6M	MatterGen Density	Prefix	[Density, $E_{\text{hull}}^{\text{PBE}}$]
CrystalLLM- π COD-XRD	IID2	Open-Source	47.7M	COD XRD	Residual	$[20 \times 2\theta, 20 \times intensity]$
CrystalLLM- π SLME	IΙΕ	Open-Source	38.7M	MP SLME	Prefix	[SLME]

Table XI. Overview of open sourced CrystaLLM- π model variants. This table summarises the models released in relation with this work, detailing their specific training datasets, parameter counts, and the architectural method used to incorporate property conditioning. While all models developed are available upon request, these are the most performant models for each main study in this work which may be useful for the community. The models can be found on the paper's Hugging Face repository

M. XRD analysis for TiO₂ polymorphs

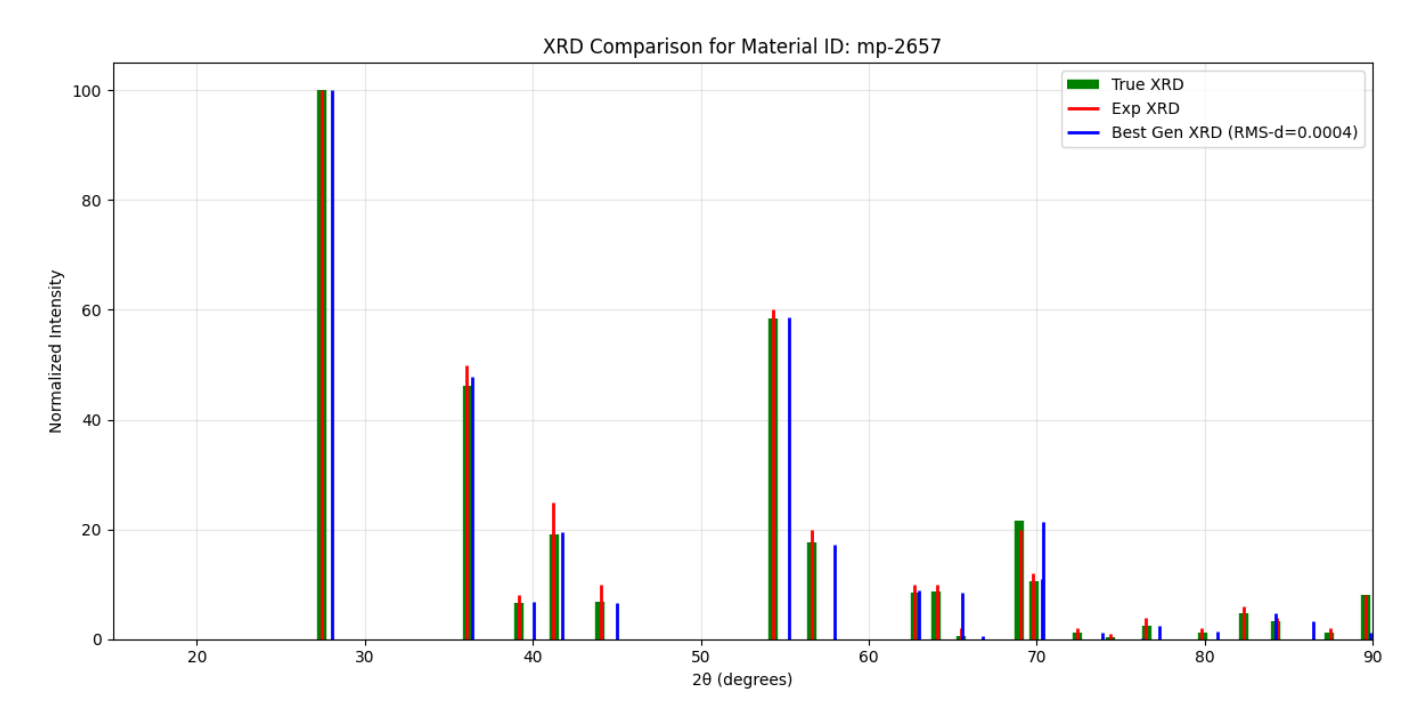


Figure 12. XRD patterns for the experimental data (red - which serves as the conditioning vector) against the theoretical XRD pattern for the best generated structure (blue) in Section II D 2, and the theoretical XRD of the 'true' structure that we match to (green - the rutile structure in the materials project database, mp-2657). The results show the light divergence between experimental and theoretical XRDs which the model has to account for during inference.

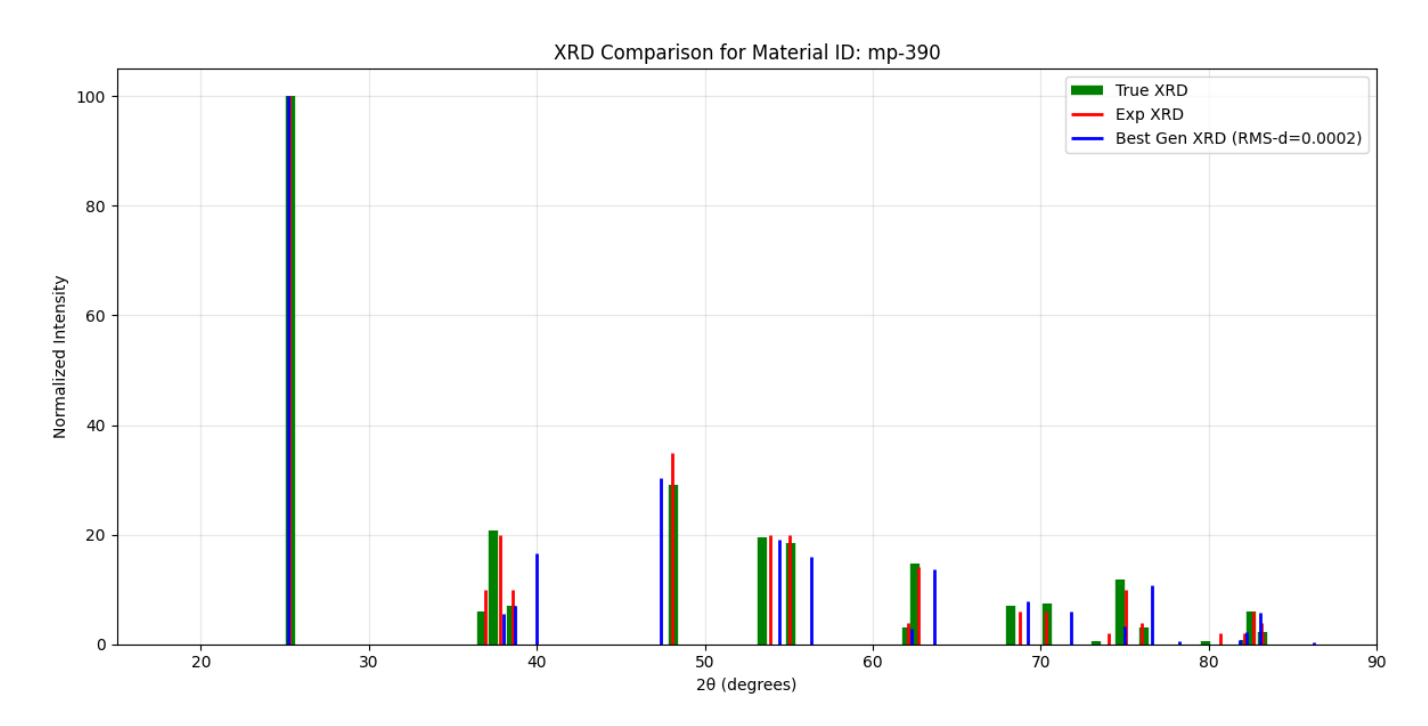


Figure 13. XRD patterns for the experimental data (red - which serves as the conditioning vector) against the theoretical XRD pattern for the best generated structure (blue) in Section II D 2, and the theoretical XRD of the 'true' structure that we match to (green - the anatase structure in the materials project database, mp-390). The results show the divergence between experimental and theoretical XRDs which the model has to account for during inference.

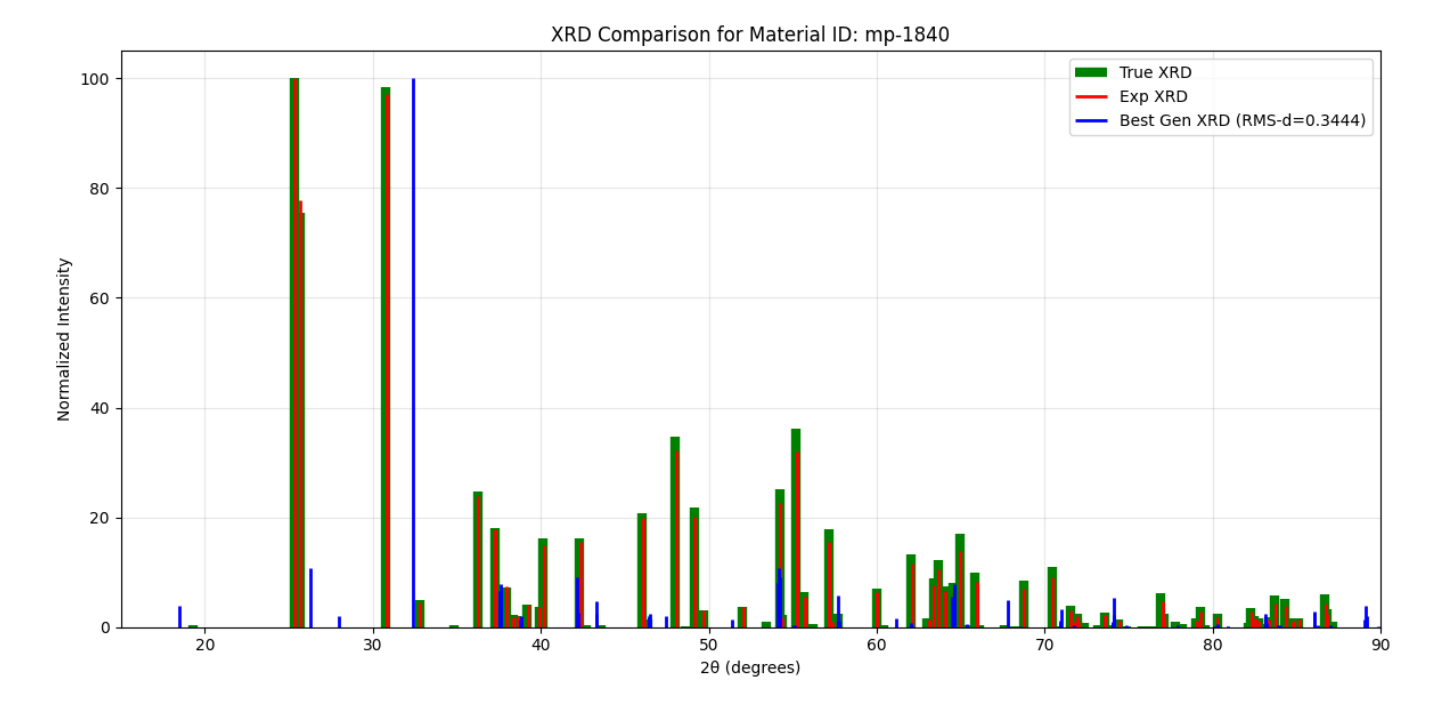


Figure 14. XRD patterns for the experimental data (red - which serves as the conditioning vector, although here over 20 peaks are present, meaning only the 20 most intense were used to condition the model) against the theoretical XRD pattern for the best generated structure (blue) in Section II D 2, and the theoretical XRD of the 'true' structure that we match to (green - the brookite structure in the materials project database, mp-1840). The results show the divergence between experimental and theoretical XRDs which the model has to account for during inference.

N. SLME Candidate Structures

Reduced	Pred.	Sustainability	Novelty	MACE	DFT	DFT	Outcome / Status
Formula	SLME (%)	(HHI_{dist})	(Str. Comp.)	$E_{ m hull}$	$E_{ m hull}$	SLME (%)	
			Condition: H	ligh SLME O	ptimisation		
Cs ₃ (GeBr ₃) ₄	30.8	7224	ft-pt ft-pt	0.040	_	_	Excluded: Unusual oxidation states
$\mathbf{Rb}_2(\mathbf{NbCl}_3)_3$	30.4	7203	ft ft	0.021	0.003	11.6	Validated: Stable
$\mathbf{Rb}_2(\mathbf{NbCl}_3)_3$	29.9	7203	ft ft	0.015	0.003	11.3	Validated: Stable
$\mathbf{Rb}_2(\mathbf{NbBr}_3)_3$	29.8	8747	ft-pt ft-pt	0.017	0.001	13.25	Validated: Stable
$Cs_2(NbCl_3)_3$	28.9	7344	ft ft	-0.011	_	_	Excluded: Structural Redundancy
$Ba_{3}GaAs_{3}$	28.5	4361	ft-pt ft	0.086	-	-	Excluded: Structural Redundancy
CsSnTe ₂	28.4	5724	ft-pt ft	0.072	-0.329	Metallic	Interested: but DFT showed metallic
TaTeI ₃	28.4	6166	ft ft	0.024	-	-	Excluded: Unusual oxidation states
Cs ₂ NaInAs ₂	28.1	6298	ft ft	-0.070	-0.605	26.4	Validated: High Efficiency and Stable
TaI ₆	28.1	6512	ft-pt ft	0.016	_	-	Excluded: Unusual oxidation states
Ba ₄ Bi ₂ O	27.9	5502	ft ft	0.015	_	_	Excluded: Low Novelty
K_3InAs_2	27.9	5204	ft ft	-0.013	_	_	Excluded: Structural Redundancy
$Cs_2NaGaAs_2$	27.9	6731	ft ft	-0.042	-0.589	24.4	Validated: High Efficiency and Stable
$K_2NaSnSb_2$	27.9	6198	ft ft	0.000	0.035	Metallic	Interested: but DFT showed metallic
$Cs_2NaSnAs_2$	27.8	6114	ft ft	0.008	_	_	Excluded: Structural Redundancy
		Condition	: Combined Sustain	ability (HHI	list) and SLM	AE Optimisation	
KAg ₃ S ₂	25.5	2207	ft None	0.045	_	_	Excluded: Low Novelty
Cu_3GeS_4	25.8	2440	ft ft	-0.032	-	-	Excluded: Low Novelty
KCu_3S_2	25.2	2574	ft-pt ft	0.029	_	-	Excluded: Chemical Heuristics (Cu-II)
SnS	25.5	2644	ft-pt None	0.057	-	-	Excluded: Known Material
Ba(CuS) ₂	25.8	2656	ft None	0.057	-	-	Excluded: Low Novelty
$K_2Ni_3S_4$	25.4	2706	ft None	0.001	-	-	Excluded: Low Novelty
$K_2(TiCl_3)_3$	27.1	2748	ft ft	0.026	_	-	Excluded: Unusual oxidation states
$K_2(TiCl_3)_3$	26.0	2748	ft ft	0.018	_	-	Excluded: Unusual oxidation states
$K_2(TiCl_3)_3$	26.5	2748	ft ft	0.022	_	_	Excluded: Unusual oxidation states
Cu ₂ SiSe ₄	26.0	2794	ft-pt ft	0.047	_	_	Excluded: Chemical Heuristics (Cu-II)
$K_2Cu_3S_4$	26.4	2797	ft-pt ft-pt	0.064	0.183	Metallic	Interested: but DFT showed metallic
NaHfCuS ₃	25.1	2886	ft ft	-0.076	-0.013	23.3	Validated: High Efficiency and Stable
Ba(CuSe) ₂	26.2	2974	ft None	0.045	-	_	Excluded: Low Novelty
KCu ₂ Se ₃	26.9	3014	ft-pt ft	0.052	_	_	Excluded: Chemical Heuristics (Cu-II)
KCu_2Se_3	26.3	3014	ft ft	0.048	-	_	Excluded: Chemical Heuristics (Cu-II)

Table XII. Screening summary of the top 30 generated photovoltaic candidates sorted by their conditioning metric. **Bold** entries denote candidates that have been validated via DFT to be stable or high-efficiency, and entries with outcome status in *italics* show materials that were further investigated using DFT but did not end up satisfactory. The top panel lists candidates conditioned purely on optimal SLME (> 30%), while the bottom panel targets a multi-objective condition of high SLME and low Supply Chain Risk (as per Methods IV E). **Novelty** is categorised as novel with respect to fine-tuning data (ft) or both fine-tuning and pre-training data (ft-pt). 'Unusual oxidation states' exclusions refer to elements cases where unusual oxixdation states of some elements are required for charge balancing. Cu(II) containing compounds are excluded due to d⁹ copper being difficult to treat accurately with DFT. E_{hull} values are reported in eV/atom. As per the original paper from Yu and Zunger, a material was considered of high efficiency above a threshold of 20%[61].

- [1] A. K. Cheetham, R. Seshadri, and F. Wudl, Chemical synthesis and materials discovery, Nature Synthesis 1, 514 (2022).
- [2] D. Antypov, A. Vasylenko, C. Collins, L. Daniels, G. Darling, M. Dyer, J. Claridge, and M. Rosseinsky, Discovery of crystalline inorganic solids in the digital age, Accounts of chemical research 58, 1355 (2025).
- [3] A. Merchant, S. Batzner, S. S. Schoenholz, M. Aykol, G. Cheon, and E. D. Cubuk, Scaling deep learning for materials discovery, Nature 624, 80 (2023).
- [4] D. W. Davies, K. T. Butler, A. J. Jackson, A. Morris, J. M. Frost, J. M. Skelton, and A. Walsh, Computational screening of all stoichiometric inorganic materials, Chem 1, 617 (2016).
- [5] F. Tiwari, Exploring the World of Functional Materials Revolutionizing Technology and Beyond, Advanced Materials Science Research **6**, 1 (2023).
- [6] U. Nwabara, K. Yang, A. Talekar, V. Bernales, J. González, S. Miller, and J. Wu, High throughput computational and experimental methods for accelerated electrochemical materials discovery, Journal of Materials Chemistry A 13, 26041 (2025).
- [7] Z. Allahyari and A. R. Oganov, Coevolutionary search for optimal materials in the space of all possible compounds, npj Computational Materials 6, 55 (2020).
- [8] K. T. Butler, D. W. Davies, H. Cartwright, O. Isayev, and A. Walsh, Machine learning for molecular and materials science, Nature **559**, 547 (2018).
- [9] G. Hautier, Finding the needle in the haystack: Materials discovery and design through computational ab initio high-throughput screening, Computational Materials Science **163**, 108 (2019).
- [10] J. Armstrong, A. J. O'Malley, M. R. Ryder, and K. T. Butler, Understanding dynamic properties of materials using neutron spectroscopy and atomistic simulation, Journal of Physics Communications 4, 072001 (2020).
- [11] H. Park, Z. Li, and A. Walsh, Has generative artificial intelligence solved inverse materials design?, Matter 7, 2355 (2024).
- [12] B. Sanchez-Lengeling and A. Aspuru-Guzik, Inverse molecular design using machine learning: Generative models for matter engineering, Science 361, 360 (2018).
- [13] P.-P. De Breuck, H.-C. Wang, G.-M. Rignanese, S. Botti, and M. A. Marques, Generative ai for crystal structures: A review, arXiv preprint arXiv:2509.02723 (2025).
- [14] T. Xie, X. Fu, O.-E. Ganea, R. Barzilay, and T. Jaakkola, Crystal Diffusion Variational Autoencoder for Periodic Material Generation (2022), arXiv:2110.06197 [cs].
- [15] H. Park, A. Onwuli, and A. Walsh, Exploration of crystal chemical space using text-guided generative artificial intelligence (2024).
- [16] N. Gruver, A. Sriram, A. Madotto, A. G. Wilson, C. L. Zitnick, and Z. W. Ulissi, Fine-tuned language models generate stable inorganic materials as text, in *International Conference on Learning Representations* 2024 (2024).
- [17] B. K. Miller, R. T. Q. Chen, A. Sriram, and B. M. Wood, FlowMM: Generating Materials with Riemannian Flow Matching (2024), arXiv:2406.04713 [cs].
- [18] T. Pakornchote, N. Choomphon-anomakhun, S. Arrerut, C. Atthapak, S. Khamkaeo, T. Chotibut, and T. Bovornratanaraks, Diffusion probabilistic models enhance variational autoencoder for crystal structure generative modeling (2023), arXiv:2308.02165 [cs].
- [19] R. Jiao, W. Huang, P. Lin, J. Han, P. Chen, Y. Lu, and Y. Liu, Crystal Structure Prediction by Joint Equivariant Diffusion (2024), arXiv:2309.04475 [cond-mat].
- [20] R. Jiao, W. Huang, Y. Liu, D. Zhao, and Y. Liu, Space Group Constrained Crystal Generation (2024), arXiv:2402.03992 [cs].
- [21] A. Klipfel, Y. Frégier, A. Sayede, and Z. Bouraoui, Vector field oriented diffusion model for crystal material generation, Proceedings of the AAAI Conference on Artificial Intelligence (2024).
- [22] D. Levy, S. S. Panigrahi, S.-O. Kaba, Q. Zhu, K. L. K. Lee, M. Galkin, S. Miret, and S. Ravanbakhsh, SymmCD: Symmetry-Preserving Crystal Generation with Diffusion Models (2025), arXiv:2502.03638 [cond-mat].
- [23] F. Cornet, F. Bergamin, A. Bhowmik, J. M. G. Lastra, J. Frellsen, and M. N. Schmidt, Kinetic Langevin Diffusion for Crystalline Materials Generation (2025), arXiv:2507.03602 [cs].
- [24] R. Chang, A. Pak, A. Guerra, N. Zhan, N. Richardson, E. Ertekin, and R. P. Adams, Space group equivariant crystal diffusion, arXiv preprint arXiv:2505.10994 (2025).
- [25] T. M. Nguyen, S. A. Tawfik, T. Tran, S. Gupta, S. Rana, and S. Venkatesh, Hierarchical gflownet for crystal structure generation, in *AI for Accelerated Materials Design-NeurIPS 2023 Workshop* (2023).
- [26] C.-Y. Ye, H.-M. Weng, and Q.-S. Wu, Con-CDVAE: A method for the conditional generation of crystal structures, Computational Materials Today 1, 100003 (2024).
- [27] X. Luo, Z. Wang, P. Gao, J. Lv, Y. Wang, C. Chen, and Y. Ma, Deep learning generative model for crystal structure prediction, npj Computational Materials 10, 254 (2024).
- [28] X. Luo, Z. Wang, Q. Wang, J. Lv, L. Wang, Y. Wang, and Y. Ma, CrystalFlow: A Flow-Based Generative Model for Crystalline Materials (2025), arXiv:2412.11693 [cond-mat].
- [29] S. Yang, K. Cho, A. Merchant, P. Abbeel, D. Schuurmans, I. Mordatch, and E. D. Cubuk, Scalable Diffusion for Materials Generation (2024), arXiv:2311.09235 [cs].
- [30] C. Zeni, R. Pinsler, D. Zügner, A. Fowler, M. Horton, X. Fu, Z. Wang, A. Shysheya, J. Crabbé, S. Ueda, R. Sordillo, L. Sun, J. Smith, B. Nguyen, H. Schulz, S. Lewis, C.-W. Huang, Z. Lu, Y. Zhou, H. Yang, H. Hao, J. Li, C. Yang, W. Li, R. Tomioka, and T. Xie, A generative model for inorganic materials design, Nature 639, 1 (2025).
- [31] K. Yan, X. Li, H. Ling, K. Ashen, C. Edwards, R. Arroyave, M. Zitnik, H. Ji, X. Qian, X. Qian, and S. Ji, Invariant Tokenization of Crystalline Materials for Language Model Enabled Generation, in *The Thirty-eighth Annual Conference on Neural Information Processing Systems* (2024).

- [32] Z. Cao, X. Luo, J. Lv, and L. Wang, Space Group Informed Transformer for Crystalline Materials Generation, https://arxiv.org/abs/2403.15734v2 (2024).
- [33] T. Mohanty, M. Mehta, H. M. Sayeed, B. Oded, I. Pitussi, A. Borenstein, V. Srikumar, and T. D. Sparks, CrysText: A Generative AI Approach for Text-Conditioned Crystal Structure Generation using LLM (2025).
- [34] P.-P. D. Breuck, H. A. Piracha, G.-M. Rignanese, and M. A. L. Marques, A generative material transformer using Wyckoff representation (2025), arXiv:2501.16051 [cond-mat].
- [35] N. Kazeev, W. Nong, I. Romanov, R. Zhu, A. Ustyuzhanin, S. Yamazaki, and K. Hippalgaonkar, Wyckoff transformer: Generation of symmetric crystals, URL https://arxiv. org/abs/2503.02407 (2025).
- [36] N. Alampara, S. Miret, and K. M. Jablonka, Mattext: Do language models need more than text & scale for materials modeling?, arXiv preprint arXiv:2406.17295 (2024).
- [37] A. Vaswani, N. Shazeer, N. Parmar, J. Uszkoreit, L. Jones, A. N. Gomez, L. Kaiser, and I. Polosukhin, Attention Is All You Need (2023), arXiv:1706.03762.
- [38] K. Choudhary, AtomGPT: Atomistic Generative Pretrained Transformer for Forward and Inverse Materials Design, The Journal of Physical Chemistry Letters 15, 6909 (2024).
- [39] Y. Xia, P. Jin, S. Xie, L. He, C. Cao, R. Luo, G. Liu, Y. Wang, Z. Liu, Y.-J. Chen, Z. Guo, Y. Bai, P. Deng, Y. Min, Z. Lu, H. Hao, H. Yang, J. Li, C. Liu, J. Zhang, J. Zhu, K. Wu, W. Zhang, K. Gao, Q. Pei, Q. Wang, X. Liu, Y. Li, H. Zhu, Y. Lu, M. Ma, Z. Wang, T. Xie, K. Maziarz, M. Segler, Z. Yang, Z. Chen, Y. Shi, S. Zheng, L. Wu, C. Hu, P. Dai, T.-Y. Liu, H. Liu, and T. Qin, NatureLM: Deciphering the Language of Nature for Scientific Discovery (2025), arXiv:2502.07527 [cs].
- [40] K. Choudhary, DiffractGPT: Atomic Structure Determination from X-ray Diffraction Patterns using Generative Pre-trained Transformer (2024).
- [41] K. M. Jablonka, P. Schwaller, A. Ortega-Guerrero, and B. Smit, Leveraging Large Language Models for Predictive Chemistry (2023).
- [42] A. A. Levy and M. Geva, Language Models Encode Numbers Using Digit Representations in Base 10 (2025), arXiv:2410.11781 [cs].
- [43] H. Li, X. Chen, Z. XU, D. Li, N. Hu, F. Teng, Y. Li, L. Qiu, C. J. Zhang, Q. Li, and L. Chen, Exposing Numeracy Gaps: A Benchmark to Evaluate Fundamental Numerical Abilities in Large Language Models (2025), arXiv:2502.11075 [cs].
- [44] J. Schmidt, T. F. Cerqueira, A. H. Romero, A. Loew, F. Jäger, H.-C. Wang, S. Botti, and M. A. Marques, Improving machine-learning models in materials science through large datasets, Materials Today Physics 48, 101560 (2024).
- [45] Martin Siron, Inel Djafar, Lucile Ritchie, Etienne Du-Fayet, Amandine Rossello, Ali Ramlaoui, Leandro von Werra, Thomas Wolf, and Alexandre Duval, Lemat-bulkunique dataset (2024).
- [46] S. Kirklin, J. E. Saal, B. Meredig, A. Thompson, J. W. Doak, M. Aykol, S. Rühl, and C. Wolverton, The Open Quantum Materials Database (OQMD): Assessing the accuracy of DFT formation energies, npj Computational Materials 1, 15010 (2015).
- [47] A. Sriram, B. K. Miller, R. T. Chen, and B. M. Wood, Flowllm: Flow matching for material generation with large language models as base distributions, URL https://arxiv.org/abs/2410.23405 (2024).
- [48] L. M. Antunes, K. T. Butler, and R. Grau-Crespo, Crystal structure generation with autoregressive large language modeling, Nature Communications 15, 10570 (2024).
- [49] A. Radford, J. Wu, R. Child, D. Luan, D. Amodei, and I. Sutskever, *Language Models are Unsupervised Multitask Learners*, Tech. Rep. (OpenAI, 2019).
- [50] X. L. Li and P. Liang, Prefix-Tuning: Optimizing Continuous Prompts for Generation (2021), arXiv:2101.00190 [cs].
- [51] M. McCloskey and N. J. Cohen, Catastrophic Interference in Connectionist Networks: The Sequential Learning Problem, in *Psychology of Learning and Motivation*, Vol. 24, edited by G. H. Bower (Academic Press, 1989) pp. 109–165.
- [52] E. J. Hu, Y. Shen, P. Wallis, Z. Allen-Zhu, Y. Li, S. Wang, L. Wang, and W. Chen, LoRA: Low-Rank Adaptation of Large Language Models (2021), arXiv:2106.09685 [cs].
- [53] K. D. M. Harris, M. Tremayne, and B. M. Kariuki, Contemporary Advances in the Use of Powder X-Ray Diffraction for Structure Determination, Angewandte Chemie International Edition **40**, 1626 (2001).
- [54] H. M. Rietveld, A profile refinement method for nuclear and magnetic structures, Journal of Applied Crystallography 2, 65 (1969).
- [55] S. Lu, H. Lin, L. Yao, Z. Gao, X. Ji, W. E, L. Zhang, and G. Ke, Uni-3DAR: Unified 3D Generation and Understanding via Autoregression on Compressed Spatial Tokens (2025), arXiv:2503.16278 [cs].
- [56] Q. Li, R. Jiao, L. Wu, T. Zhu, W. Huang, S. Jin, Y. Liu, H. Weng, and X. Chen, Powder diffraction crystal structure determination using generative models, Nature Communications 16, 7428 (2025).
- [57] A. Jain, S. P. Ong, G. Hautier, W. Chen, W. D. Richards, S. Dacek, S. Cholia, D. Gunter, D. Skinner, G. Ceder, and K. A. Persson, Commentary: The Materials Project: A materials genome approach to accelerating materials innovation, APL Materials 1, 011002 (2013).
- [58] K. Choudhary, K. F. Garrity, A. C. E. Reid, B. DeCost, A. J. Biacchi, A. R. H. Walker, Z. Trautt, J. Hattrick-Simpers, A. G. Kusne, A. Centrone, A. Davydov, J. Jiang, R. Pachter, G. Cheon, E. Reed, A. Agrawal, X. Qian, V. Sharma, H. Zhuang, S. V. Kalinin, B. G. Sumpter, G. Pilania, P. Acar, S. Mandal, K. Haule, D. Vanderbilt, K. Rabe, and F. Tavazza, The Joint Automated Repository for Various Integrated Simulations (JARVIS) for data-driven materials design, npj Computational Materials 6, 10.1038/s41524-020-00440-1 (2020), arXiv:2007.01831 [cond-mat].
- [59] M. M. Martirossyan, T. Egg, P. Hoellmer, G. Karypis, M. Transtrum, A. Roitberg, M. Liu, R. G. Hennig, E. B. Tadmor, and S. Martiniani, All that structure matches does not glitter (2025), arXiv:2509.12178 [cs].
- [60] W. Shockley and H. J. Queisser, Detailed Balance Limit of Efficiency of p-n Junction Solar Cells, Journal of Applied Physics 32, 510 (1961).
- [61] L. Yu and A. Zunger, Identification of Potential Photovoltaic Absorbers Based on First-Principles Spectroscopic Screening of Materials, Physical Review Letters 108, 068701 (2012).
- [62] M. Walker and K. T. Butler, The carbon cost of materials discovery: Can machine learning really accelerate the discovery of new photovoltaics? (2025), arXiv:2507.13246 [cond-mat].
- [63] J. H. Song, H. Choi, H. T. Pham, and S. Jeong, Energy level tuned indium arsenide colloidal quantum dot films for efficient photovoltaics,

- Nature Communications 9, 4267 (2018).
- [64] N. Papež, R. Dallaev, Ş. Ţălu, and J. Kaštyl, Overview of the Current State of Gallium Arsenide-Based Solar Cells, Materials 14, 3075 (2021).
- [65] J. Dias, M. Andrade, and L. Mascaro, Chapter 13 chalcogenide compounds for solar cells, in *Green Sustainable Process for Chemical and Environmental Engineering and Science*, edited by Inamuddin, R. Boddula, A. M. Asiri, and M. M. Rahman (Elsevier, 2021) pp. 245–270.
- [66] K. Kuhar, A. Crovetto, M. Pandey, K. S. Thygesen, B. Seger, P. C. Vesborg, O. Hansen, I. Chorkendorff, and K. W. Jacobsen, Sulfide perovskites for solar energy conversion applications: computational screening and synthesis of the selected compound lays 3, Energy & Environmental Science 10, 2579 (2017).
- [67] A. Q. Jiang, A. Sablayrolles, A. Mensch, C. Bamford, D. S. Chaplot, D. de las Casas, F. Bressand, G. Lengyel, G. Lample, L. Saulnier, L. R. Lavaud, M.-A. Lachaux, P. Stock, T. L. Scao, T. Lavril, T. Wang, T. Lacroix, and W. E. Sayed, Mistral 7B (2023), arXiv:2310.06825 [cs].
- [68] R. Novak, Y. Bahri, D. A. Abolafia, J. Pennington, and J. Sohl-Dickstein, Sensitivity and Generalization in Neural Networks: An Empirical Study (2018), arXiv:1802.08760 [stat].
- [69] H. Fang, S. Tao, N. Chen, K.-X. Chang, and T. Sakai, Do Large Language Models Favor Recent Content? A Study on Recency Bias in LLM-Based Reranking (2025), arXiv:2509.11353 [cs].
- [70] Z. Li, S. Liu, B. Ye, D. J. Srolovitz, and T. Wen, Active Learning for Conditional Inverse Design with Crystal Generation and Foundation Atomic Models (2025), arXiv:2502.16984 [cond-mat].
- [71] Qwen, A. Yang, B. Yang, B. Zhang, B. Hui, B. Zheng, B. Yu, C. Li, D. Liu, F. Huang, H. Wei, H. Lin, J. Yang, J. Tu, J. Zhang, J. Yang, J. Yang, J. Zhou, J. Lin, K. Dang, K. Lu, K. Bao, K. Yang, L. Yu, M. Li, M. Xue, P. Zhang, Q. Zhu, R. Men, R. Lin, T. Li, T. Tang, T. Xia, X. Ren, X. Ren, Y. Fan, Y. Su, Y. Zhang, Y. Wan, Y. Liu, Z. Cui, Z. Zhang, and Z. Qiu, Qwen2.5 Technical Report (2025), arXiv:2412.15115 [cs].
- [72] J. Su, Y. Lu, S. Pan, A. Murtadha, B. Wen, and Y. Liu, RoFormer: Enhanced Transformer with Rotary Position Embedding (2023), arXiv:2104.09864 [cs].
- [73] K. Clark, U. Khandelwal, O. Levy, and C. D. Manning, What Does BERT Look At? An Analysis of BERT's Attention (2019), arXiv:1906.04341 [cs].
- [74] J. Vig, A Multiscale Visualization of Attention in the Transformer Model (2019), arXiv:1906.05714 [cs].
- [75] A. Templeton, T. Conerly, J. Marcus, J. Lindsey, T. Bricken, B. Chen, A. Pearce, C. Citro, E. Ameisen, A. Jones, H. Cunningham, N. L. Turner, C. McDougall, M. MacDiarmid, C. D. Freeman, T. R. Sumers, E. Rees, J. Batson, A. Jermyn, S. Carter, C. Olah, and T. Henighan, Scaling monosemanticity: Extracting interpretable features from claude 3 sonnet, Transformer Circuits Thread (2024).
- [76] I. Loshchilov and F. Hutter, Decoupled Weight Decay Regularization (2019), arXiv:1711.05101 [cs].
- [77] J. Howard and S. Ruder, Universal Language Model Fine-tuning for Text Classification, https://arxiv.org/abs/1801.06146v5 (2018).
- [78] A. Fan, M. Lewis, and Y. Dauphin, Hierarchical Neural Story Generation (2018), arXiv:1805.04833 [cs].
- [79] A. Holtzman, J. Buys, L. Du, M. Forbes, and Y. Choi, The Curious Case of Neural Text Degeneration, in *International Conference on Learning Representations* (2019).
- [80] S. P. Ong, W. D. Richards, A. Jain, G. Hautier, M. Kocher, S. Cholia, D. Gunter, V. L. Chevrier, K. A. Persson, and G. Ceder, Python Materials Genomics (pymatgen): A robust, open-source python library for materials analysis, Computational Materials Science 68, 314 (2013).
- [81] K. Choudhary and B. DeCost, Atomistic Line Graph Neural Network for improved materials property predictions, npj Computational Materials 7, 185 (2021).
- [82] J. P. Perdew, K. Burke, and M. Ernzerhof, Generalized Gradient Approximation Made Simple, Physical Review Letters 77, 3865 (1996).
- [83] J. Heyd, G. E. Scuseria, and M. Ernzerhof, Hybrid functionals based on a screened Coulomb potential, The Journal of Chemical Physics 118, 8207 (2003), _eprint: https://pubs.aip.org/aip/jcp/article-pdf/118/18/8207/19093575/8207_1_online.pdf.
- [84] S. Kim, M. Lee, C. Hong, Y. Yoon, H. An, D. Lee, W. Jeong, D. Yoo, Y. Kang, Y. Youn, and S. Han, A band-gap database for semiconducting inorganic materials calculated with hybrid functional, Scientific Data 7, 387 (2020).
- [85] I. Batatia, P. Benner, Y. Chiang, A. M. Elena, D. P. Kovács, J. Riebesell, X. R. Advincula, M. Asta, M. Avaylon, W. J. Baldwin, F. Berger, N. Bernstein, A. Bhowmik, S. M. Blau, V. Cărare, J. P. Darby, S. De, F. D. Pia, V. L. Deringer, R. Elijošius, Z. El-Machachi, F. Falcioni, E. Fako, A. C. Ferrari, A. Genreith-Schriever, J. George, R. E. A. Goodall, C. P. Grey, P. Grigorev, S. Han, W. Handley, H. H. Heenen, K. Hermansson, C. Holm, J. Jaafar, S. Hofmann, K. S. Jakob, H. Jung, V. Kapil, A. D. Kaplan, N. Karimitari, J. R. Kermode, N. Kroupa, J. Kullgren, M. C. Kuner, D. Kuryla, G. Liepuoniute, J. T. Margraf, I.-B. Magdău, A. Michaelides, J. H. Moore, A. A. Naik, S. P. Niblett, S. W. Norwood, N. O'Neill, C. Ortner, K. A. Persson, K. Reuter, A. S. Rosen, L. L. Schaaf, C. Schran, B. X. Shi, E. Sivonxay, T. K. Stenczel, V. Svahn, C. Sutton, T. D. Swinburne, J. Tilly, C. van der Oord, E. Varga-Umbrich, T. Vegge, M. Vondrák, Y. Wang, W. C. Witt, F. Zills, and G. Csányi, A foundation model for atomistic materials chemistry (2024), arXiv:2401.00096 [physics].
- [86] J. Riebesell, R. E. A. Goodall, P. Benner, Y. Chiang, B. Deng, G. Ceder, M. Asta, A. A. Lee, A. Jain, and K. A. Persson, A framework to evaluate machine learning crystal stability predictions, Nature Machine Intelligence 7, 836 (2025).
- [87] G. Kresse and J. Hafner, Ab initio molecular dynamics for liquid metals, Physical Review B 47, 558 (1993).
- [88] G. Kresse and J. Furthmüller, Efficiency of ab-initio total energy calculations for metals and semiconductors using a plane-wave basis set, Computational Materials Science 6, 15 (1996).
- [89] G. Kresse and J. Hafner, Norm-conserving and ultrasoft pseudopotentials for first-row and transition elements, Journal of Physics: Condensed Matter 6, 8245 (1994).
- [90] G. Kresse and D. Joubert, From ultrasoft pseudopotentials to the projector augmented-wave method, Phys. Rev. B 59, 1758 (1999).
- [91] A. M. Ganose, H. Sahasrabuddhe, M. Asta, K. Beck, T. Biswas, A. Bonkowski, J. Bustamante, X. Chen, Y. Chiang, D. C. Chrzan, J. Clary, O. A. Cohen, C. Ertural, M. C. Gallant, J. George, S. Gerits, R. E. A. Goodall, R. D. Guha, G. Hautier, M. Horton, T. J. Inizan, A. D. Kaplan, R. S. Kingsbury, M. C. Kuner, B. Li, X. Linn, M. J. McDermott, R. S. Mohanakrishnan, A. N. Naik, J. B. Neaton, S. M. Parmar,

- K. A. Persson, G. Petretto, T. A. R. Purcell, F. Ricci, B. Rich, J. Riebesell, G.-M. Rignanese, A. S. Rosen, M. Scheffler, J. Schmidt, J.-X. Shen, A. Sobolev, R. Sundararaman, C. Tezak, V. Trinquet, J. B. Varley, D. Vigil-Fowler, D. Wang, D. Waroquiers, M. Wen, H. Yang, H. Zheng, J. Zheng, Z. Zhu, and A. Jain, Atomate2: modular workflows for materials science, Digital Discovery 4, 1944 (2025).
- [92] D. H. Fabini, M. Koerner, and R. Seshadri, Candidate inorganic photovoltaic materials from electronic structure-based optical absorption and charge transport proxies, Chemistry of Materials 31, 1561 (2019).
- [93] M. W. Gaultois, T. D. Sparks, C. K. H. Borg, R. Seshadri, W. D. Bonificio, and D. R. Clarke, Data-Driven Review of Thermoelectric Materials: Performance and Resource Considerations, Chemistry of Materials 25, 2911 (2013).
- [94] D. W. Davies, K. T. Butler, A. J. Jackson, J. M. Skelton, K. Morita, and A. Walsh, Smact: Semiconducting materials by analogy and chemical theory, Journal of Open Source Software 4, 1361 (2019).
- [95] R. Woods-Robinson, Y. Xiong, J.-X. Shen, N. Winner, M. K. Horton, M. Asta, A. M. Ganose, G. Hautier, and K. A. Persson, Designing transparent conductors using forbidden optical transitions (2023), arXiv:2303.16994 [cond-mat].
- [96] S. Gražulis, D. Chateigner, R. T. Downs, A. F. T. Yokochi, M. Quirós, L. Lutterotti, E. Manakova, J. Butkus, P. Moeck, and A. Le Bail, Crystallography Open Database an open-access collection of crystal structures, Journal of Applied Crystallography 42, 726 (2009).
- [97] T. Akiba, S. Sano, T. Yanase, T. Ohta, and M. Koyama, Optuna: A Next-generation Hyperparameter Optimization Framework (2019), arXiv:1907.10902 [cs, stat].